NON-DESTRUCTIVE DETECTION OF WOODY BREAST MYOPATHY IN BROILER BREAST FILLETS BY EMERGING OPTICAL IMAGING TECHNOLOGIES

By

Jiaxu Cai

A THESIS

Submitted to
Michigan State University
in partial fulfillment of the requirements
for the degree of

Biosystems Engineering – Master of Science

2024

ABSTRACT

Woody breast (WB), one of the major muscular myopathies in poultry, impairs the quality and marketability of poultry products, leading to significant economic losses for poultry industries worldwide due to product downgrading and consumer complaints. WB-affected broiler breast fillets are characterized by abnormal tissue hardness, muscle rigidity, and irregular shape profiles. Manual evaluation based on tactile palpation and visual examination is the current practice for WB assessment at poultry processing facilities, but it is subjective, labor-intensive, and may cause contamination or safety concerns due to physical contact for evaluation. This thesis aimed to investigate the applicability of two emerging optical imaging technologies, i.e., 1) light scattering imaging (LSI) and 2) sinusoidal illumination reflectance imaging (SIRI), under both broadband and multispectral modes, for assessing WB myopathy in broiler breast fillets. The corresponding broadband and multispectral images were collected using custom-assembled imaging platforms from broiler meat samples of varying WB conditions, respectively. Different types of features were extracted from the resultant images (i.e., scattering images and demodulated SIRI images) and then utilized for discriminant modeling to classify samples into two [i.e., "Normal (no WB)" and "Defective"] and three [i.e., "Normal (no WB)", "Moderate", "Severe"] categories according to WB conditions. Two imaging technologies, i.e., LSI and SIRI, implemented in both broadband and multispectral modes have shown promising potential for the detection of WB defects in broiler breast fillets. More research is needed to further enhance the performance of WB assessment.

This work is dedicated to my parents and grandparents.

ACKNOWLEDGEMENTS

First, I am sincerely grateful to my graduate advisor, Dr. Yuzhen Lu, for his continuous guidance, encouragement, understanding, and patience throughout my two years of M.S. study at Michigan State University. Without his support, I would not have been able to complete this work. I also appreciate my committee members: Dr. Renfu Lu, Dr. Daniel Morris, and Dr. Xue Zhang, for their valuable feedback on my research works, which has greatly helped me build my professionalism as an early-career researcher.

My sincere thanks also go to the Department of Biosystems and Agricultural Engineering at Michigan State University, a warm, supportive, and welcoming BAE family, that has allowed me to enjoy my research while having a fulfilling time outside of work. I am also grateful to my undergraduate advisor in China, Dr. Yuwei Wang, for his step-by-step guidance in helping me start my research career successfully.

I appreciate all my lab mates – Dr. Yibin Wang, Dr. Jiajun Xu, Boyang Deng, Dr. Xinyang Mu, Yuyuan Tian, and Jiaming Zhang – for their valuable advice on my project. I also thank my friends and office mates, Meicai Xu, Dingqiang Ye, Wanqun Yang, Emeka Aniekwensi, Abraham Rai, Greg Rouland, Karim Aldekhail, for their companionship and understanding. In particular, I would like to thank Kun (Iris) Teng and Moxuan (Lilly) Li for their friendship during our travels in Mexico, which brought me a rare sense of peace and created memories I will cherish forever.

Last but not least, I would like to express my deepest gratitude and love to my grandparents, Fengming Cai and Fuyi Liu, my parents, Li Wang and Tianlong Cai, and other family members for their years of understanding and moral support throughout my study.

TABLE OF CONTENTS

LIST OF SYMBOLS AND ABBREVIATIONS

2-D	Two-Dimensional
3-D	Three- Dimensional
AC	Amplitude Component
BIA	Bioelectrical Impedance Analysis
BMORS	Blunt Meullenet-Owens Razor Shear
DC	Direct Component
DL	Deep Learning
EF	Expressible Fluid
FC	Fully Connected
LD	Lorentzian Distribution
LSI	Light Scattering Imaging
MLD	Modified Lorentzian Distribution
MORS	Meullenet-Owens Razor Shear
MRMR	Minimum Redundancy Maximum Relevance
NIA	Numerical Integration Area
NIR	Near-Infrared
NIRS	Near-Infrared Spectroscopy
OCT	Optical Coherence Tomography
PCA	Principal Component Analysis
PCs	Principal Components
RLDA	Regularized Linear Discriminant Analysis
SIRI	Sinusoidal Illumination Reflectance Imaging

SM	Spaghetti Meat
SVM	Support Vector Machine
VIS	Visible
WB	Woody Breast
WS	White Striping

CHAPTER 1: INTRODUCTION

1.1 Poultry Industry

Poultry meat is a primary source of animal proteins and essential nutrients such as vitamins, iron, zinc (Marangoni et al., 2015). The global demand for poultry products has steadily increased in recent years due to their affordability and associated health benefits (Ellsworth et al., 2023). In the United States (U.S.), per capita consumption of poultry meat has grown from 82.9 lbs to 99.5 lbs over the past decade and is projected to increase to 107.5 lbs by 2033 (NCC, 2022a). To meet the growing demand for poultry meat, intense genetic selection of broilers has been implemented over decades, enabling substantial increases in growth rate, weight gain, and feed efficiency (USDA-ERS, 2024).

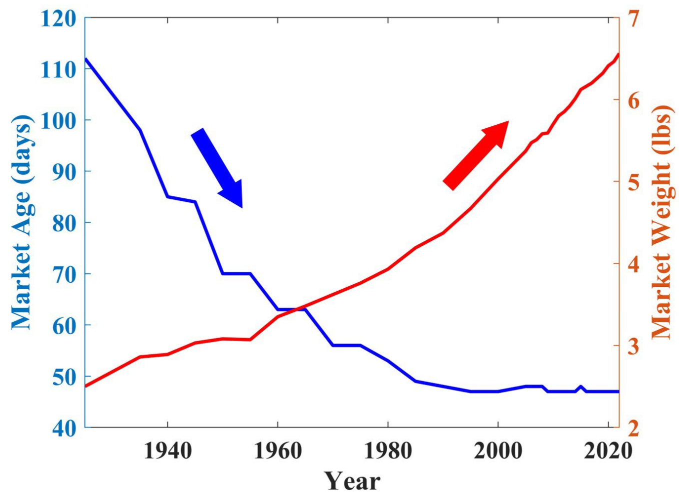

Figure 1.1. Broiler performance in the United States: market age and weight from 1925 – 2023 (NCC, 2022b).

As shown in Figure 1.1, the average size and weight of broilers on the market have doubled over the past 30 years for exceptional growth performance and breast meat yield (NCC, 2022b). However, the rapid growth of broilers has brought about the prevalence of muscular myopathies or defects in poultry meat (Petracci et al., 2015; Tijare et al., 2016), such as woody breast, white striping, and spaghetti meat (Che et al., 2022). These myopathies impair the quality and consumer acceptance of poultry products (da Silva et al., 2017), leading to an annual loss of hundreds of millions of dollars for the U.S. poultry industry (Barbut, 2019).

1.2 Woody Breast (WB) Myopathy and Instrumental Measurement

WB, which is among the most challenging quality issues in the global poultry industry, is a muscle anomaly characterized by abnormal tissue hardness, muscle rigidity, and irregular shape profiles (Caldas-Cueva & Owen, 2020), along with elevated levels of fibrosis, collagen, lipidosis, etc. (Sihvo et al., 2014; Soglia et al., 2016), although the etiology remains to be fully ascertained. Previous studies have reported a high incidence of WB in broiler fillets of about 60%-90%, influenced by factors such as flocks, dietary treatments, bird age, and among others (de Almeida Mallmann, 2019; Tijare et al., 2016; Xing et al., 2020; Barbut, 2019). Currently, at commercial poultry processing facilities, WB assessment is done manually based on hand palpation combined with visual examination by trained personnel (Figure 2.1) (Pang et al., 2020; Dalgaard et al., 2018). This approach is labor-intensive, costly, and prone to human assessment errors.

Instrumental texture analysis methods (Xiong et al., 2006; Morey & Owens, 2017), such as Meullenet-Owens razor shear (MORS), blunt MORS (BMORS), and Warner-Bratzler shear, have been applied to correlate physical measurements (e.g., peak count, shear force, energy) with WB conditions (Bowker & Zhuang, 2019). In Yang et al. (2021), an expressible fluid (EF) measurement method, which employs external force to press a sample of defined size onto filter paper to extract water or juice, was investigated for predicting degrees of WB conditions in broiler breast fillets, resulting in an accuracy of 93.3% in classifying samples into three WB degrees. However, these approaches above are destructive, time-consuming, and thus not suited for online detection of bulk samples.

Siddique et al. (2021, 2022) performed the bioelectrical impedance analysis (BIA) as a non-destructive method to assess WB conditions in broiler breast meat, obtaining accuracies of 66.7%-88.9% in differentiating normal and defective samples using support vector machines (SVM) algorithm. The performance of BIA depended on the severity of WB degree (i.e., normal, moderate, and severe) and instrument configurations (i.e., hand-held and plate BIA). Parajuli et al. (2024) reported on the use of a force-sensing robot device to characterize the spatial distribution of WB in broiler fillets based on compression force measurements. Either the BIA or force sensing approach has noticeable limitations given the requirement of close contact with samples, which is susceptible to food contamination, relatively slow for sample evaluation, and hence may not be preferred for in-line detection. Sun et al. (2021) applied an active air-deformation system, originally developed for tenderness evaluation of poultry meats based on shape deformation analysis (Lee et al., 2008), to assess WB conditions in broiler fillets, where the best correlation coefficient of -0.86 was achieved between deformation diameter (i.e., D15) and WB categories (i.e., normal, mild, and severe). Despite these investigations, since no imaging technology was involved, the lack of or limited spatial information acquired on poultry samples could hinder the effective discrimination between normal and myopathic samples.

1.3 Computer Vision and Optical Sensing Technology

Computer vision or imaging technology has received widespread attention in meat quality evaluation (Taheri-Garavand et al., 2019; Modzelewska-Kapituła & Jun, 2022; Park, 2016), with a handful of recent studies on WB assessment. Caldas-Cueva et al. (2021) reported an accuracy of 84% for distinguishing normal from WB-affected broiler carcasses using color images. A small set of the features describing carcass structural information (e.g., length, width, area, etc.) were extracted and modeled using logistic regression analysis, in which broiler carcasses affected by WB showed greater breast width at cranial and caudal regions ($P < 0.05$) as well as greater angles at the tip of keel and breast areas in the caudal section ($P < 0.05$). Yoon et al. (2022) developed a side-view machine vision system for online detection of WB-affected broiler breast fillets, where the muscle rigidity and bending characteristics of each sample fillet were analyzed. Three different conveyor speeds of 10-100 feet per second were tested, and an average overall accuracy of about 95% was achieved in classifying two-class (normal vs defective) samples. These studies demonstrated the relevance of sample geometric morphology (e.g., dimensions, bending curvature, etc.) to WB assessment, although there was room for improvement in differentiating between moderate and severe WB categories.

Yoon et al., (2016) and Ekramirad et al. (2024) employed optical coherence tomography (OCT) to image the subsurface tissues of broiler meats for WB detection, achieving an overall accuracy of 95% for differentiating normal and WB-affected samples. It is noted that OCT is a mesoscopic imaging modality that acquires information from small sample areas, e.g., 5 mm × 1.7 mm (lateral × depth) in Ekramirad et al. (2024), which could be limited in characterizing the spatial heterogeneity of poultry samples.

Other optical sensing technologies have been also investigated for poultry quality assessment. Wold et al. (2017, 2019) used near-infrared spectroscopy (NIRS) to assess WB conditions of broiler fillets, where a commercial 15-band NIR scanning system [QVision500 (TOMRA Sorting Solutions, Leuven, Belgium)] originally used for meat chemical composition analysis was adapted for online WB detection. The NIR scanner yielded an accuracy of 91.1% in classifying normal and WB-affected chicken samples, while a separate benchtop NIRS instrument achieved a higher accuracy of 96.6% (Wold & Løvland, 2020). Geronimo et al. (2019) utilized NIRS combined with a computer vision system for classifying normal and WB-affected breast samples, obtaining overall accuracies of 96.3% and 91.8%, respectively; however, the limited number of samples (40 normal and 40 defective) used in their research may result in unreliable performance evaluations. Li et al. (2022) applied NIRS and compression speed models for WB detection and obtained an accuracy of 82.58% and 82.14% in recognizing normal and WB-affected samples, respectively. NIRS is well suited for online applications, but as a point sensing technique, it acquires information from a small area, which may restrict its detection capacity; currently, few NIRS units are commercially adopted by poultry industries (Barbut et al., 2024).

Recently, Pallerla et al. (2024) reported using line-scanning hyperspectral imaging in the spectral range of 400-1,000 nm for classifying fillet samples of three WB degrees ("normal", "mild WB", and "severe WB"), obtaining an overall accuracy of 95%. However, conventional line-scanning hyperspectral imaging still faces challenges with lengthy image acquisition and processing for online food inspection (Lu et al., 2020b). There is a continuing interest in advancing imaging technology to effectively detect WB in chicken fillets for enhanced quality assessment.

1.4 Light Scattering Imaging (LSI)

Chicken meat affected by WB myopathy has altered tissue structure and composition (Sihvo et al., 2014; Soglia et al., 2016), such as an increase in degenerative and atrophic fibers and elevated levels of fibrosis, collagen, lipidosis, and necrosis as well as harder texture. These WB-associated lesions imply a change in optical properties, especially light scattering (Vishwanath et al., 2009; Birth, 1978; Birth et al., 1978; Qin & Lu, 2007), compared to normal tissues. Since optical scattering indicates structural/textural characteristics of tissues (Vishwanath et al., 2009; Birth et al., 1978), imaging technology that enhances light scattering measurements would be conceivably useful for WB assessment.

Early research into light scattering imaging (LSI) of foods was focused on fruit firmness prediction (McGlone et al., 1997; Cho & Han, 1999; Tu et al., 2000; Noh & Lu, 2007). For instance, Lu (2004a, 2004b) extracted spatial scattering profiles extracted from scattering images of apples for firmness prediction. In subsequent work, Peng & Lu (2006a, 2006b, 2006c, 2007, 2008) proposed a modified, four-parameter Lorentzian distribution function to characterize scattering profiles for predicting the firmness and soluble solids content of apples. A handful of studies were reported on the use of LSI for meat quality evaluation (Xia et al., 2008; Ranasinghesagara et al., 2010). In Cluff et al. (2008, 2013) and Wu et al. (2012), LSI in hyperspectral mode was employed for classifying beef samples based on tenderness. Hyperspectral scattering imaging was also utilized to assess pork tenderness (Sun et al., 2019a) and freshness (Li et al., 2016). Despite these prior studies, to the best of our knowledge, there has been a lack of research on the use of LSI for assessing myopathic defects such as WB in poultry. Moreover, few studies have systematically engineered features of scattering images for model development.

1.5 Sinusoidal Illumination Reflectance Imaging (SIRI)

Sinusoidal illumination reflectance imaging (SIRI), which employs spatially modulated light in the sinewave form for sample imaging, is capable of depth-resolved characterization for enhanced tissue defect detection as well as three-dimensional (3-D) surface reconstruction (Lu & Cai, 2024), which can be difficult to achieve by conventional uniform illumination imaging. In SIRI, acquired pattern images are demodulated into two sets of intensity images, i.e., direct component (DC) and amplitude component (AC) (Lu et al., 2016a); DC corresponds to the image due to uniform illumination, while AC is unique to sinusoidally modulated structured light, which provides better contrast and resolution for physical features, depending on the spatial frequency of illumination patterns (Lu & Lu, 2019). Numerous studies demonstrated the effectiveness of SIRI for enhanced detection of defects in horticultural products, such as bruises in apples (Lu et al., 2016b; Lu & Lu, 2017, 2018a, 2018b; Li et al., 2018), chilling injury in cucumbers (Lu & Lu, 2020; Lu & Lu, 2021; Lu et al., 2021), and early decay in peaches (Sun et al., 2019b) and oranges (Li et al., 2023, 2024).

Recently, the application of SIRI in broadband, panchromatic imaging mode was extended to meat products (Olaniyi et al., 2023a, 2023b, 2024; Cai et al., 2024). In assessing white striping (WS) in chicken fillets, a muscular defect characterized by white striations on meat surface/subsurface, AC images resulted in consistently better accuracies with improvements up to 12% or higher compared to DC images, depending on modeling approaches (Olaniyi et al., 2023b). In SIRI, because light patterns projected onto samples are deformed by the sample geometry, such deformation can be utilized for 3-D surface reconstruction on a pixel level using demodulated phase images combined with existing profilometry techniques in optical metrology (Zhang, 2018a; Zuo et al., 2018), as demonstrated in a study on surface profiling of apples (Lu & Lu, 2018c). WB-affected chicken fillets tend to exhibit ridge-like bulges along the cranial to caudal region varying with severities of WB, as opposed to normal (WB-free) fillets that have relatively flat and uniform shape profiles (Caldas-Cueva & Owen, 2020; Kuttappan et al., 2016). Additionally, WB-affected fillets are often affected by WS defects due to the interrelated histological changes in the affected muscle tissues (Bowker et al., 2019; Aguirre et al., 2020). These characteristics of WB make SIRI potentially effective for WB assessment of poultry breast fillets given the demonstrated efficacy of the imaging technique for surface geometry profiling of samples (Lu & Lu, 2018c) and WS detection of poultry meat (Olaniyi et al., 2023a, 2023b). To the best of our knowledge, no research has been carried out on the feasibility and potential of SIRI for poultry WB assessment.

1.6 Hypothesis and Objectives

WB impairs poultry products' quality, consumer acceptance, and marketability, leading to significant economic loss for the U.S. poultry industry and beyond. Appropriate inspection technology has yet to be implemented at the processing line for objective, non-contact, and automated detection of WB conditions in poultry meat, enabling product grading, sorting, and value-added processing. LSI and SIRI are two emerging optical imaging technologies that have received significant attention for quality detection in horticultural products. This study was built upon the hypothesis that the application of LSI and SIRI can be applied to poultry products for enhanced assessment of WB conditions in broiler breast fillets.

The study is to investigate the applicability of emerging LSI and SIRI in detecting WB conditions in broiler breast meat. Specific objectives of the research are to:

1) Conduct quantitative texture measurement of samples using a texture analyzer (Chapter 2);
2) Acquire images from chicken fillets of varying WB conditions using custom-assembled imaging platforms under a highly focused light beam and sinusoidal illumination, respectively (Chapters 2 and 3);
3) Develop algorithm pipelines that extract features from broadband images (i.e., scattering image and demodulated SIRI images) for classifying samples into two and three WB categories (Chapters 2 and 3);
4) Upgrade broadband LSI and SIRI systems into multispectral mode for potentially improved WB assessment (Chapter 4);
5) Evaluate the efficacy of LSI and SIRI in different modes (i.e., broadband and multispectral) for WB assessment in broiler breast fillets.

CHAPTER 2: DETECTION OF WOODY BREAST CONDITION IN BROILER BREAST FILLETS USING LIGHT SCATTERING IMAGING

2.1 Broiler Breast Samples

A total of 242 broiler breast fillets were collected in three batches from the deboning line of a commercial poultry processing plant (Orland, IN, USA), with sample sizes of 75 (10/20/2023), 80 (01/04/2024), and 87 (05/09/2024) per sampling, respectively, which was to ensure that experiments on each batch could be completed within two months and therefore to minimize potential quality degradation during cold storage. The broiler fillets were assessed by trained personnel at the processing facility and classified into three categories by WB conditions: 95 "Normal", 72 "Moderate", and 75 "Severe" samples, based on hand palpation and visual examination. Figure 2.1 shows photographs taken during poultry sampling.

Figure 2.1. Broiler breast fillets sampled and evaluated at a commercial poultry processing plant (Orland, IN, USA).

These fillets were packed in coolers filled with ice and immediately transported to the laboratory for this study. Upon arrival, they were further evaluated to correct potential errors in categorization, and then individually packed in a foam tray, wrapped in film, and stored in a freezer at -20 °C before image collection. The frozen samples were transferred to cold storage at around 2 °C for 24-48 hours prior to imaging to allow them to thaw. The effects of the freeze-thaw process on the broiler samples were not considered in this study (Villegas-Cayllahua et al., 2023; Soglia et al., 2019). Figure 2.2 shows photographs of representative broiler meat samples of three WB conditions [i.e., “Normal (no WB)”, “Moderate”, and “Severe”], where the two defective samples are characterized by an out-bulging shape profile at the cranial and caudal ends varying with the severity of WB, as compared with the normal (no WB) one.

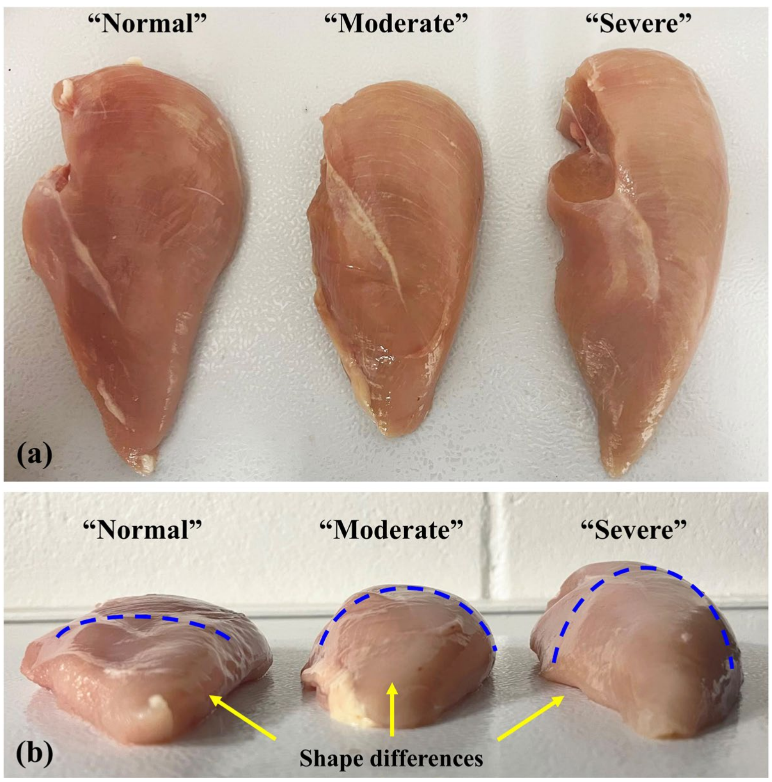

Figure 2.2. (a) Front and (b) side views of example broiler breast fillets of three woody breast (WB) conditions, i.e., “Normal (no WB)”, “Moderate”, “Severe”.

2.2 Texture Measurement

Right after image collection (described in Session 2.3 and 3.1), each sample was weighted and subjected to texture analysis using a texture analyzer (TA.XT2i, Stable Micro Systems, Surrey, UK), equipped with a blunt Meullenet-Owens razor shear (BMORS) probe. The texture analysis provided quantitative measures of samples in terms of the shear force (N) and energy (N.mm). The samples were sheared seven times by the BMORS probe on the ventral surface at the cranial region (Bowker & Zhuang, 2019; Pang et al., 2020) with a test speed of 5 mm/s, pre- and post-speed of 10 mm/s, and a trigger force of 10 g, up to a maximum puncture depth of 20 mm (Figure 2.3). Table 2.1 summarizes the instrumental measurements of broiler fillets used in this study. The WB-affected samples had higher values of shear force and energy compared to normal (non-WB) samples, which agrees with previous observations on WB assessment (Bowker & Zhuang, 2019; Sun et al., 2021; Yoon et al., 2022); though, these measurements were overall lower than those previously reported, probably due to the relatively small samples (in terms of weight) collected in this study. Differences in bird strains, flocks, and meat status (e.g., fresh non-frozen vs. frozen-thawed meat) contribute to variations in texture measurements (Bowker & Zhuang, 2019; Petracci et al., 2015; Tijare et al., 2016).

Table 2.1 Statistics of the weight and texture properties (mean ± standard deviation) of broiler breast samples

	"Normal"	"Moderate"	"Severe"
Number of samples	95	72	75
Average weight (g)	194.14±69.99	267.17±54.62	292.21±41.49
Average shear force (N)	8.45±1.63	15.22±5.43	28.29±12.09
Average shear energy (N.mm)	70.69±12.98	121.96±35.18	211.13±83.9

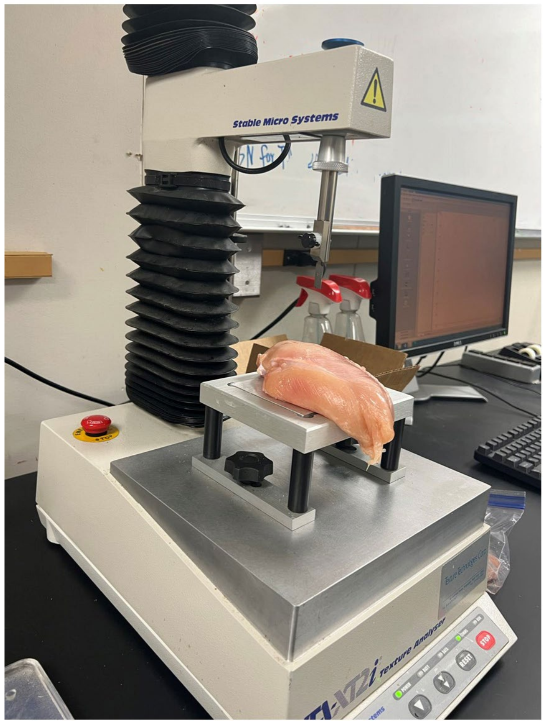

Figure 2.3. Texture analyzer with a blunt Meullenet-Owens razor shear probe used for measuring shear force (N) and energy (N.mm) of broiler meat samples.

2.3 Imaging System

A benchtop light scattering imaging (LSI) system was assembled for chicken meat imaging. It mainly consists of, as schematically shown in Figure 2.4, a computer, a high-performance monochromatic camera (Edge 4.2, PCO, Kelheim, Germany) with a resolution of 2048 × 2048 pixels, attached with a 35 mm fixed focal length lens (Edmund Optics Inc., Barrington, NJ, USA), and a broadband light source unit. The light, which was generated from a DC-regulated quartz tungsten halogen lamp (Newport Corporation, Irvine, CA, USA) alongside a radiometric power supply controller set at 500 W, passed through a visible-near-infrared optical fiber with a core size of 200 μm (Ocean Insight, Orlando, FL, USA) and a collimator to form a focused beam of about 1.8 mm in diameter at the cranial region of the chicken fillet; it induced light scattering within meat tissues, covering an apparent scattering area of about 30 mm in diameter (Figure 2.4).

The camera was positioned perpendicularly downward at about 19 cm above the sample to capture backscattered light from the sample, with a pixel resolution of about 0.03 mm/pixel. The optical fiber was angled about 10° with respect to the vertical axis and at a distance of 11 cm from the sample. The configuration including the sample-camera distance and light incident angles were kept consistent during the entire experiment to minimize influences on light scattering imaging. The illumination/imaging area of each sample was previously leveled to avoid the interference of the sample surface geometry on light scattering. The system was operated within an enclosed cabinet to avoid the interference of ambient light. It is noted that the imaging settings (e.g., light source wattage, beam size, imaging distance, exposure time, etc.) were previously determined in a preliminary imaging test to ensure effective interaction of light with meat tissues while avoiding damage to the tissues due to exposure to highly-focused lighting; though, some other settings such as beam size and exposure time were not fully optimized in this study.

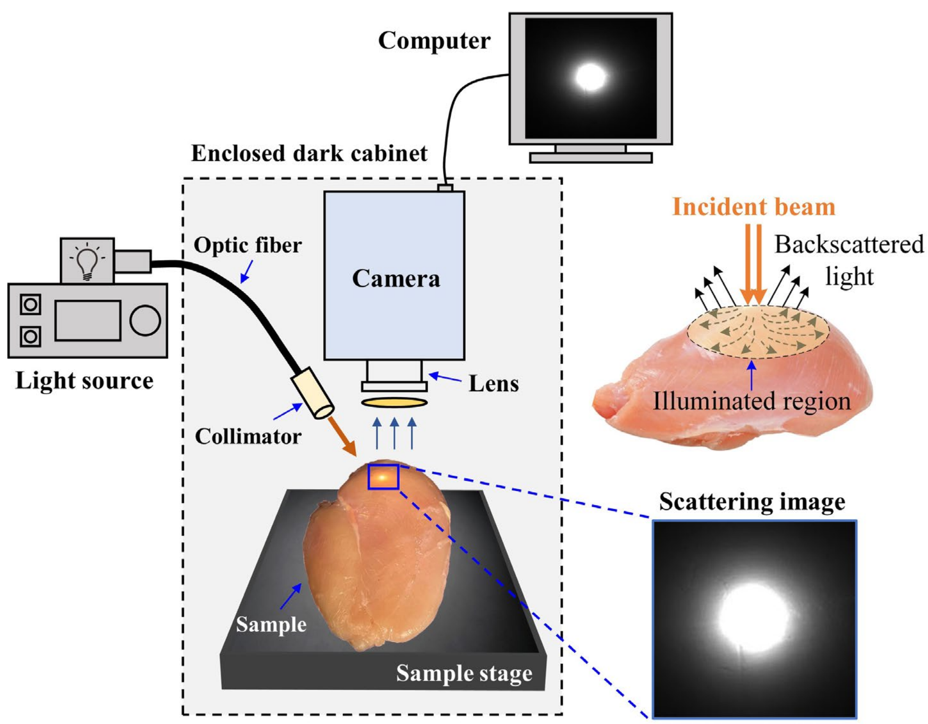

Figure 2.4. Schematic of a broadband light scattering imaging system for woody breast assessment of broiler breast meat.

Broiler meat samples were individually placed on a sample stage that allowed for vertical adjustments, ensuring consistent sample-camera distance for light scattering and image acquisition across all samples. The camera bundled software (camware v4.2, PCO, Kelheim, Germany) was used to collect images with an exposure time of 150 ms. As shown in Figure 2.4, the acquired scattering image is roughly radially symmetric to the beam incident point, and the pixel intensity outside the saturation area (i.e., the glare spot on the image) gradually decreases as the distance from the beam incident point increases, which is indicative of light scattering signals of the sample. Although the imaging measurement does not decouple the combined effect of light absorption and scattering of meat tissues, it captures typical characteristics of spatially resolved diffuse reflectance of biological tissues (Kienle et al., 1996) and provides quantitative descriptions of light scattering in the meat sample.

2.4 Feature Analysis and Classification Modeling

In this chapter, two types of features, i.e., 1) deep-learning-based and 2) hand-crafted scattering features, were extracted from scattering images for characterizing broiler samples of varying WB conditions [i.e., “Normal (no WB)”, “Moderate”, and “Severe” WB] and classification modeling. The raw scattering images (of 2048 × 2048 pixels) were used for both deep-learning and hand-crafted analyses. A pre-trained model, i.e., ResNeXt-101 (Xie et al., 2017), was applied to the scattering images for extracting features, referred to as the deep-learning-based features. The ResNeXt-101, extended from the original ResNet (He et al., 2016) with improved capabilities of learning discriminative features from images, consists of a concatenated block of 100 convolutional layers per path/cardinality, followed by a fully connected (FC) layer. To extract features by the ResNeXt-101, herein, its FC layer was discarded, and the model convolutional base was used as a feature extractor to yield a total of 2048 features from each input image. On the other hand, hand-crafted features pertinent to light scattering were extracted for model development, as opposed to the deep features by the ResNeXt-101.

As shown in Figure 2.5, the scattering image was partitioned into two areas, i.e., 1) a saturation area (SA), manifested as a glare spot, where pixel intensity reached the maximum, and 2) a light scattering (LS) area where the pixel intensity decreased to a certain percentage level of the maximum, with the source-detector distance increasing. In this chapter, the LS areas of varied sizes, with the pixel intensity attenuated to levels ranging from 50% to 5%, were considered for image analysis. Based on the visual examination of differences in scattering images between normal and defective samples, the features that describe the shape characteristics of SA and LS, which are relevant to the light scattering ability of samples, were extracted to represent the scattering images for mode development.

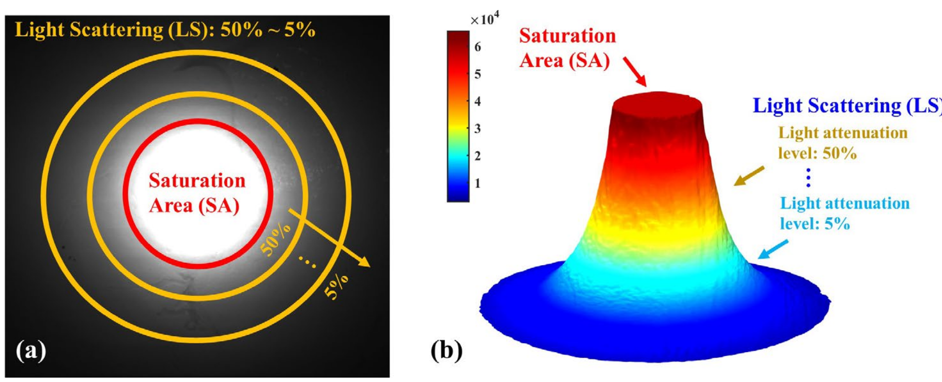

Figure 2.5. Example of a scattering image represented in (a) 2-D and (b) 3-D, consisting of a saturation area (SA) and a light scattering (LS) area of varied sizes, with the pixel intensity attenuated to levels ranging from 50% to 5%.

Moments (Gonzalez & Woods, 2018) are widely used for shape representation in pattern recognition tasks. Here, three types of moments, including 1) raw moments; 2) centralized moments; and 3) Hu-moments (Hu, 1962), were adopted for image representation and model development. The raw moments are a set of statistical measures related to the object shape, from which basic region properties such as area and centroid can be derived. Unlike raw moments, centralized moments consider the spatial distribution of pixels relative to the object centroid and are invariant to the image translation. Advanced moments, such as Hu-moments and their derivatives (Hu, 1962; Zhang et al., 2020), improve upon the basic moments and are designed to provide more robust representations that are invariant to image translation, scale, and rotation. Fourier-Descriptors offer another effective means of representing the shape of an object (Zahn & Roskies, 1972), which encodes the object contour into a set of frequency components (i.e., Fourier coefficients) through the Fourier transform. In this chapter, both moments and Fourier-Descriptors, including 24 moments (consisting of 10 raw moments, 7 centralized moments, and 7 Hu-moments) and 64 Fourier descriptors, were extracted from the SA and LS areas, respectively, yielding a total of 176 features per scattering image by concatenating them together, which is referred to as the Shape-Description features.

In previous studies of light scattering imaging of fruits, a modified Lorentzian distribution (MLD) function with four parameters was employed to represent a scattering profile, where the four parameters were estimated and then used for fruit quality assessment (Peng & Lu, 2006a, 2006b, 2006c, 2007). The Lorentzian distribution (LD) function is commonly used for describing laser profiles and light distribution patterns in optics research (Davis, 1996). Compared to the original LD, in the MLD, an additional parameter was introduced, for more accurately representing scattering profiles (Peng & Lu, 2006a, 2006b, 2006c). The MLD function is expressed as follows:

$$\mathrm{MLD} = a + \frac{b}{1+\left(x/c\right)^{d}}, \quad (x>0) \tag{2.1}$$

where x is the scattering distance, and a, b, c, and d are four parameters to be estimated. A detailed description of the MLD parameter implications is given in (Peng & Lu, 2006a, 2006b), but it is noted that only x greater than zero ($x > 0$) was used in this study for MLD fitting (Figure 2.6).

Different from previous studies (Peng & Lu, 2006a, 2006b, 2006c) that extracted one profile in two axis directions from a scattering image, in this chapter, a scattering profile was extracted from each of the four quadrants in a scattering image, as illustrated in Figure 2.6, which accounted better for the spatial inhomogeneity of light scattering characteristics of meat tissues. To obtain the scattering profile, the center of the incident beam was first identified in the scattering image, and then the image was divided into empirically determined 100 concentric circular bands with equal pixels (or distance), covering a scattering area with a light attenuation level of 10%. The scattering profile of each quadrant was obtained by averaging all pixels on the band within that quadrant, and then it was normalized by dividing the profile by its maximum. Finally, four normalized scattering profiles, with their saturation portions excluded, were fitted with the MLD respectively, resulting in a total of 16 model parameters (features) for each image.

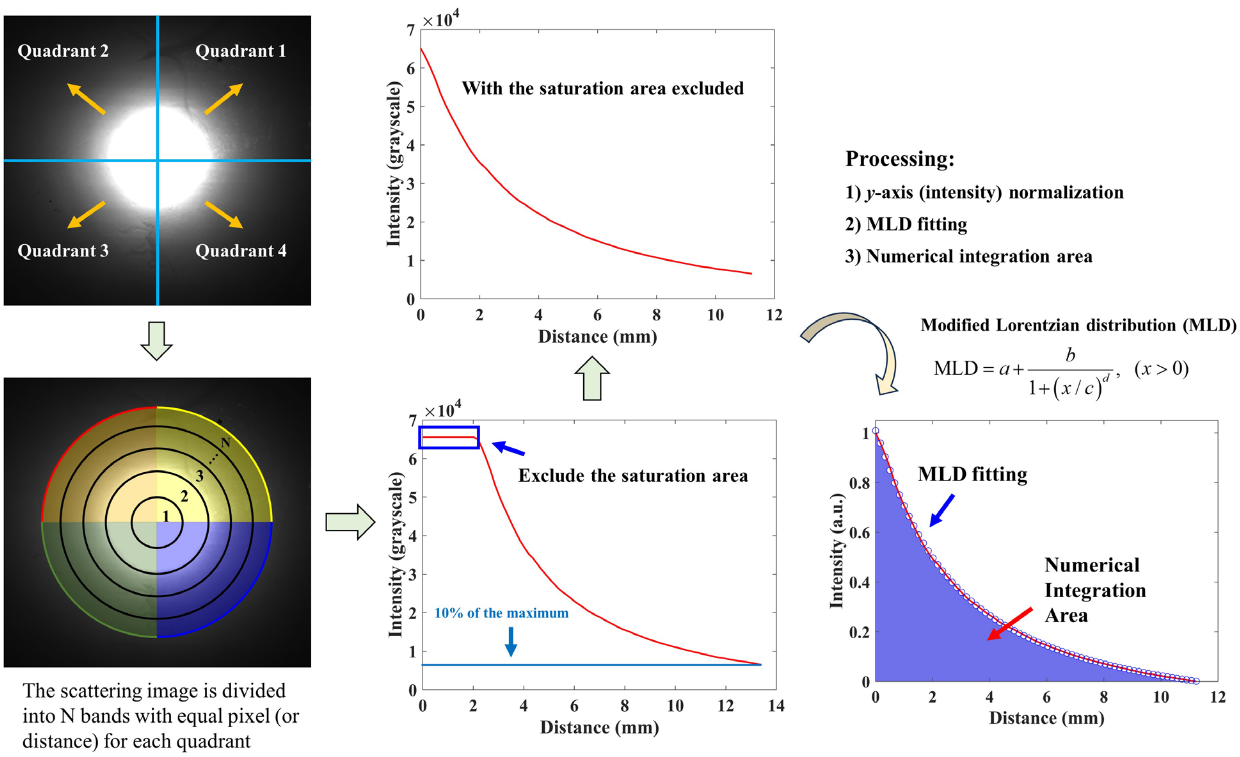

Figure 2.6. The procedures of processing a scattering image for obtaining the parameters of a modified Lorentzian distribution (MLD) function and numerical integration areas of each scattering profile within the quadrant.

Moreover, the area under the scattering profile obtained above, that is the shaded area under the curve in Figure 2.6, was calculated through numerical integration, denoted as the numerical integration area (NIA) feature. The area feature is also related to the optical scattering ability of samples and is potentially useful. Here 4 NIA features were obtained from four quadrants per image. As a result, all hand-crafted features, extracted for scattering image representation, include 1) 176 Shape-Description features, 2) 16 MLD features, and 3) 4 NIA features. Concatenating these features resulted in a total set of 196 hand-crafted features per scattering image, which would be used for sample classification.

Figure 2.7 shows the modeling pipeline for classifying broiler breast samples. The two independent sets of features, i.e., 1) deep-learning-based and 2) hand-crafted features, were employed separately for model development. The extracted feature data was randomly partitioned into training and test sets according to the ratio of 65% : 35% (corresponding to 157 : 85 fillet samples). A holdout validation with 20 replications was adopted for model training and evaluation.

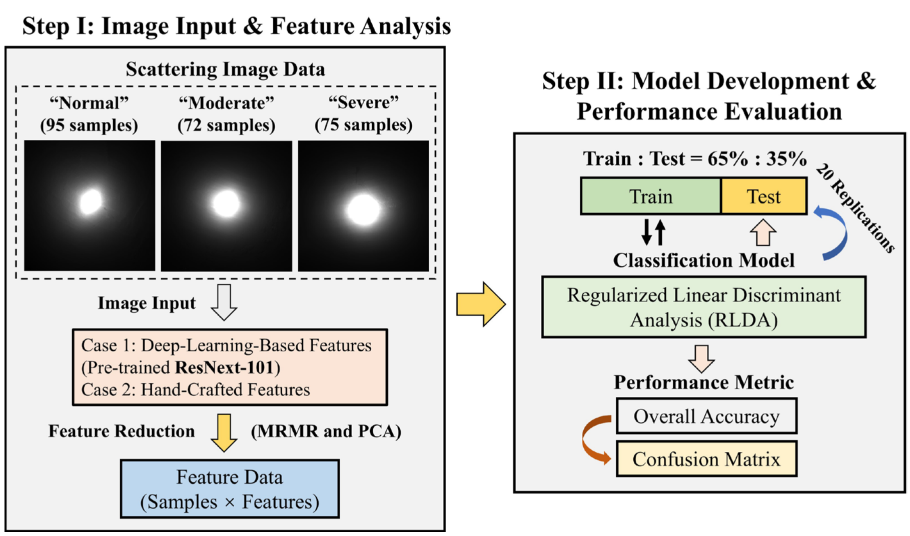

Figure 2.7. The procedures for classifying broiler breast samples into "Normal" , "Moderate", and "Severe" WB categories using the extracted features.

After the initial modeling of the two sets of features, feature reduction approaches including MRMR (minimum redundancy maximum relevance) (Ding & Peng, 2005) and PCA (principal component analysis) (Jolliffe, 2002) were applied to reduce model complexity and potentially improve classification accuracy. MRMR aimed to select a subset of features most relevant to intended tasks with the least correlation among features, while PCA was to transform the raw feature data into a small number of new variables called principal components (PCs) that explain most of the variance in the raw data. Regularized linear discriminant analysis (RLDA), which is a simple yet potent classifier for modeling high-dimensional features (Guo et al., 2007), was employed to classify poultry meat samples with the raw and reduced set of extracted features, respectively. The two tunable hyperparameters of RLDA, including the regularization parameter γ ($0 < \gamma < 1$) and the shrinkage δ ($\delta > 0$), were determined through Bayesian optimization with 10-fold cross-validation on training data in this chapter.

The performance of discriminant models was quantified in terms of overall classification accuracy and corresponding confusion matrix in 20 repeated holdout validations. Feature analysis and discriminant modeling were conducted with the aid of Matlab R2022b (The MathWorks Inc., Natick, MA, USA), PyTorch (version 1.13.1), and Scikit-learn (version 1.0.2) in Python (version 3.8.16) on a desktop computer workstation with an Intel® Core™ i9-10900x CPU (256 GB RAM) and an NVIDIA RTX A6000 GPU.

2.5 Results

2.5.1 Scattering Images and Profiles

Figure 2.8 shows example scattering images of broiler meat samples of varying WB conditions. Compared to the “Normal” (WB-free) samples, the scattering images of defective samples (affected by “Moderate” and “Severe” WB) tended to have larger saturation areas that were more radially symmetric regarding the beam incident point, varying with the severity of WB. The average saturation area size (in terms of pixel counts) of the “Normal”, “Moderate”, and “Severe” samples were 29,326±10,832, 41,695±9,563, and 48,136±7,407 pixels, respectively. In contrast, the WB-affected samples (including "Moderate" and "Severe") exhibited overall smaller scattering areas (beyond the saturation areas) than the "Normal" samples, given the same light attenuation level. The pixel intensity outside the saturation area gradually decreased as the distance from the beam incident point increased. Given the scattering area delimited by a light attenuation level of 10% of the maximum (Figure 2.6), chicken samples of "Normal", "Moderate", and "Severe" classes had average areas of 450,776±51,338, 430,366±43,186, and 409,729±39,200 pixels, respectively, although the differences among the classes were not significant. This suggests that the WB-affected samples attenuated light more rapidly in the spatial domain.

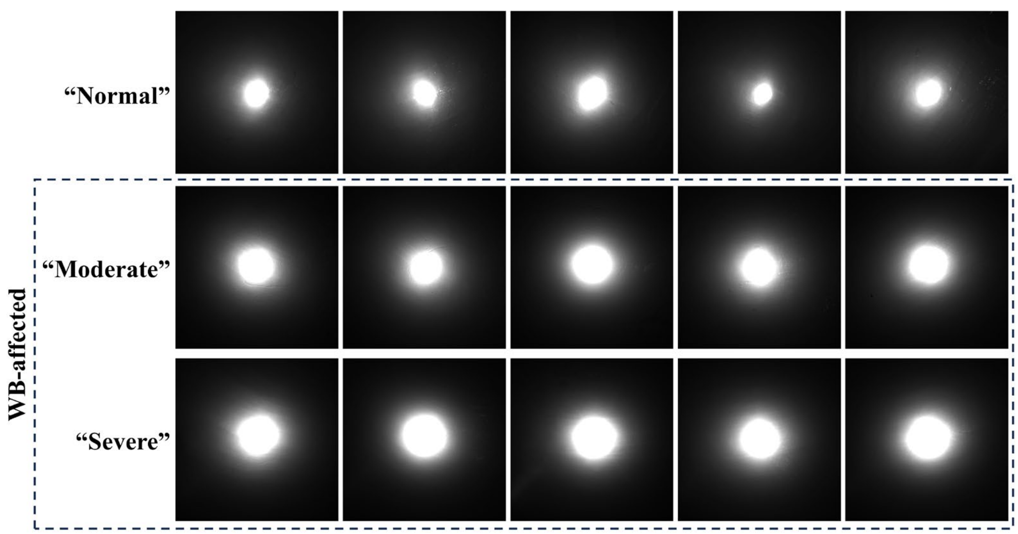

Figure 2.8. Examples of scattering images for normal and WB-affected broiler breast samples.

Figure 2.9 (a) shows the scattering profiles of samples of three WB categories extracted from the scattering areas defined at a light attenuation level of 10% of the maximum. The scattering profiles of the WB-affected samples [red and green curves in Figure 2.9 (a)] appeared to decrease more rapidly than that of the normal ones (blue curves), with the source-detector distance increasing, although the differences were subtle. These observations on scattering profiles could merit a future investigation of quantitative estimation of scattering coefficients of normal and defective samples using tissue optics approaches (Bigio & Fantini, 2016). Figure 2.9 (b) shows a scatter plot for the chicken samples visualized using the first two PCs of their scattering profiles, where PC1 and PC2 account for 89.27% and 9.09% of the total variance, respectively. The separation between normal and defective samples ("Moderate" and "Severe" combined) was present to some degree, but not clearly defined. A substantial overlap existed between the "Moderate" and the other two categories ("Normal" and "Severe"), which would complicate the differentiation between these two categories and present challenges to the overall classification of the three WB categories.

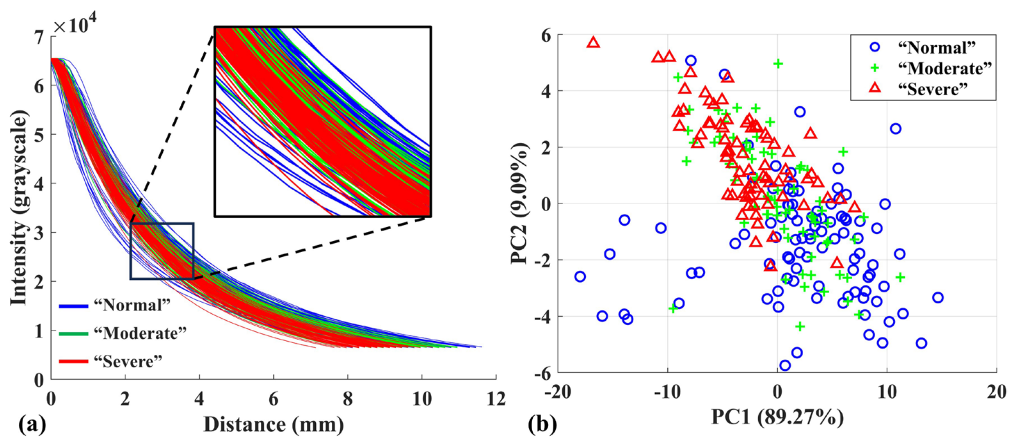

Figure 2.9. (a) Scattering profiles with the saturation portion excluded, for all normal and defective samples, i.e., "Normal", "Moderate", and "Severe"; (b) scatter plot in the space spanned by the first two principal components (PCs) for three woody breast categories of broiler breast meat samples.

2.5.2 Classification

Figure 2.10 shows the overall accuracies in classifying normal and defective (affected by "Moderate" and "Severe" WB defects) samples using the hand-crafted features extracted from the SA and LS areas of varying light attenuation levels. The LS features were extracted from the regions beyond the SA with the light attenuated to a range of 50% and 5% of its maximum intensity in a 5% decrement, to examine the effects of light attenuation levels. The performance of LS features varied with the light attenuation levels, with overall accuracies of 77.74%-85.77% and 60.6%-68.33% in 2- and 3-category classification, respectively. The combination of the features from SA and LS produced higher accuracies than those of the LS features used alone across most attenuation levels, except at 30% and 35% light attenuation levels where LS features slightly outperformed the combined features of SA and LS in either 2- or 3-category modeling scenarios, though the differences in accuracy between were not significant ($P > 0.05$). The combined features yielded overall accuracies ranging from 82.74%-85.77% and 65%-70% for 2- and 3-category WB classification, respectively (Figure 2.10).

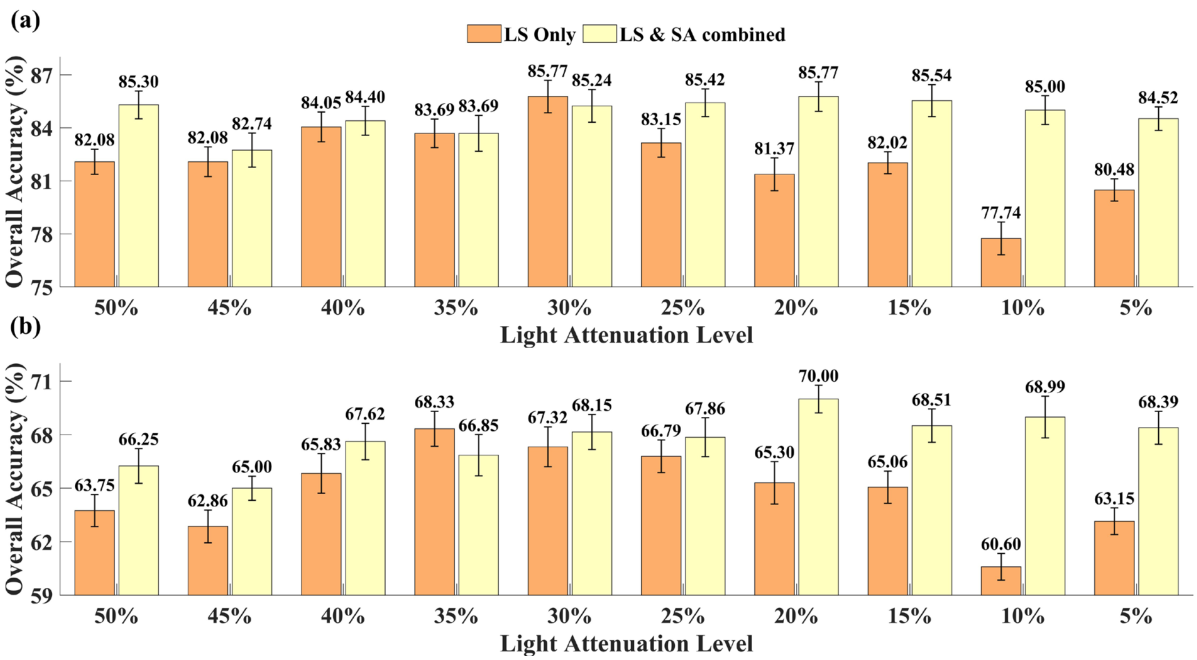

Figure 2.10. Overall accuracies of classifying broiler meat samples into (a) two (i.e., “Normal” and “Defective”) and (b) three (i.e., “Normal”, “Moderate”, and “Severe”) WB categories using the Shape-Description features extracted from the saturation area (SA) and light scattering (LS) areas delimited at varying light attenuation levels (50% - 5%), respectively.

These results suggested that the SA features contributed positively to modeling performance. The LS area at the 20% light attenuation level, although it did not yield the best classification accuracy when only LS features were modeled, produced the best accuracy (i.e., 85.77% and 70%, respectively) in both 2- and 3-category modeling when the combined features of LS and SA were used. The combined set of hand-crafted features was therefore chosen for further modeling experiments described below.

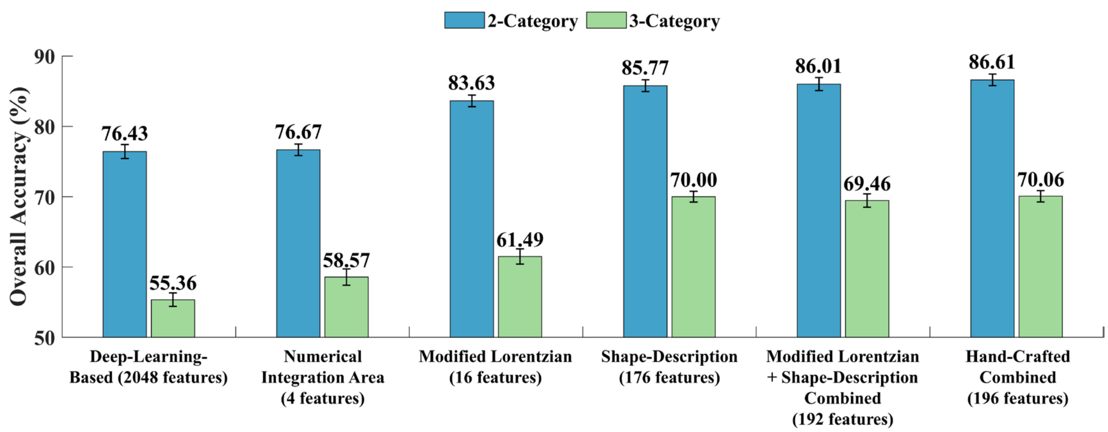

Figure 2.11. Overall accuracies of deep-learning-based and hand-crafted features in classifying broiler meat samples into two (i.e., "Normal" and "Defective") and three (i.e., "Normal", "Moderate", and "Severe") WB categories.

Figure 2.11 shows the comparison of classification performance based on deep-learning-based features and different sets of hand-crafted features. In the 2-category modeling, deep-learning-based features yielded an overall accuracy of 76.43% in differentiating between normal and defective samples, while higher accuracies of 76.67%-86.61% were obtained by hand-crafted features sets. Among the three types of hand-crafted features, as shown in Figure 2.11, the 176 Shape-Description features produced the highest accuracy of 85.77%, followed by the 16 MLD features with an accuracy of 83.63% and then 4 NIA features with an accuracy of 76.67%. Further improvements were achieved by concatenating these hand-crafted features together, yielding accuracies of 86.01% with the combination of MLD and Shape-Description features and 86.61% with a complete set of hand-crafted features, representing significant improvements ($P < 0.05$) of 9.58% and 10.18% over that obtained using deep-learning-based features, respectively. Similar results were reported in the 3-category modeling, where hand-crafted features consistently outperformed deep-learning-based features (55.36%) by a large margin, with overall improved accuracies ranging from 58.57%-70.06%. Still, the complete set of 196 hand-crafted features achieved the highest accuracy of 70.06% for the 3-category WB classification, with a significant improvement of 14.7% ($P < 0.05$) over that of deep-learning-based features.

These results demonstrate the superiority of purposely engineered features from scattering images and profiles over the features extracted by a generic "black box" deep learning model, for classifying normal and defective broiler samples. The mediocre performance of the ResNeXt-101 model is likely because this model, pre-trained on the large-scale ImageNet dataset, which consists mostly of natural scene images, was directly applied to extract features from the scattering images without any adaptation or further post-training. While the model has shown strengths in extracting certain local features (e.g., edges, corners, colors) in visual categorization tasks in the computer vision community, the ImageNet images dramatically differ from the light scattering images of chicken samples in this work, which could have restricted the transform learning performance of the ResNeXt-101, leading to the limited classification accuracy. An end-to-end deep-learning model trained from scratch on large volumes of dedicated data could deliver better performance in WB classification, which remains to be investigated in our future work.

To improve model performance, feature selection was performed on the full set of hand-crafted features. Figure 2.12 (a) shows the performance of RLDA trained using the top 5 to 195 features in a 5-feature increment, ranked by importance according to the MRMR algorithm (Ding & Peng, 2005). In 2-category modeling, the accuracy peaked at 87.92% when the top 40 features were used for modeling and then fluctuated around 85% as more features were included. With the same top 40 features, an overall accuracy of 70.24% was achieved for the 3-category WB classification and reached a maximum of 70.77% when the top 140 features were modeled. The selected features, although not fully optimized, produced slight improvements of 1.31% (2-category) and 0.71% (3-category) with reduced model complexity, compared to full-features-based modeling.

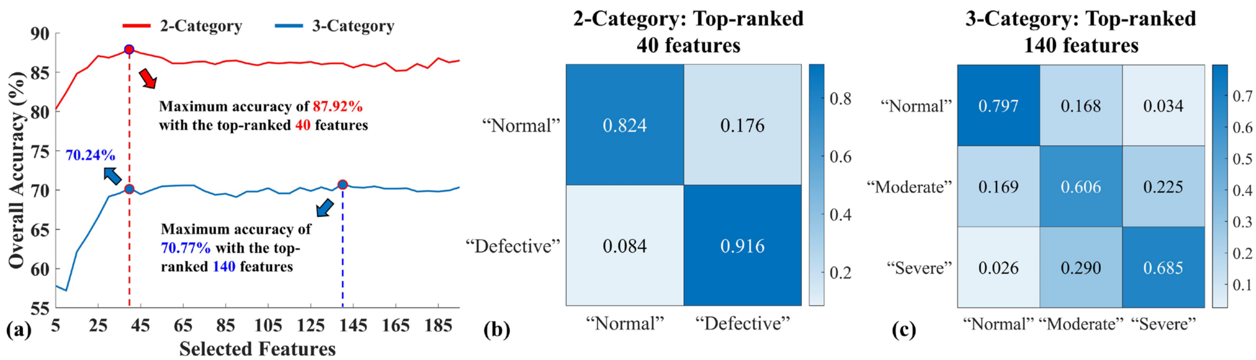

Figure 2.12. (a) Overall classification accuracies of using subsets of the most relevant hand-crafted scattering features ranked by the MRMR algorithm, ranging from 5 to 195 in an increment of 5; row-wise confusion matrices (where row and columns correspond to actual and predicted labels) for (b) two and (c) three categories modeling based on the top-ranked 40 and 140 features (best accuracy), respectively. The confusion matrix was obtained by pooling and row-wise normalizing classification results in 20 repeated holdout validations.

Figure 2.12 (b) shows the corresponding confusion matrix for the 2-category classification. The "Normal" samples contributed more to misclassifications (17.6% false negatives), with 82.4% of them correctly classified, compared to a higher accuracy of 91.6% for recognition of the "Defective" samples. In 3-category modeling, as shown in 2.12 (c), misclassifications were primarily observed between the "Moderate" and "Severe" classes, with only 60.5% and 68.5% of samples correctly classified, while the "Normal" samples were well differentiated from the WB-affected ones, especially from those of the "Severe" class, with misclassifications of less than 5% between them [i.e., 2.6% and 3.4%, Figure 2.12 (c)]. Including a larger, more balanced set of chicken samples for modeling could potentially help improve classification accuracy.

The compositions of the top 10 features ranked by MRMR, with the normalization of feature weights (corresponding to the importance), for 2- and 3-category WB classification, are shown in Figure 2.13. The two most relevant features in both 2- and 3-category modeling scenarios were the shape descriptors of the saturation area, specifically, the Hu-moments, which confirmed the importance of the saturation area of scattering images for WB assessment. The following two most relevant features in 2-category modeling were the MLD features describing the scattering profiles, and the rest of the top features were all relevant to the shape characteristics of saturation and scattering areas [Figure 2.13 (a)], while in the 3-category modeling, as illustrated in Figure 2.13 (b), all the top features, except an MLD feature, were shape-related and contributed to WB classification. This analysis indicates that shape features of SA and LS areas are important to WB assessment, and the potential of MLD features remains to be fully ascertained with further investigation.

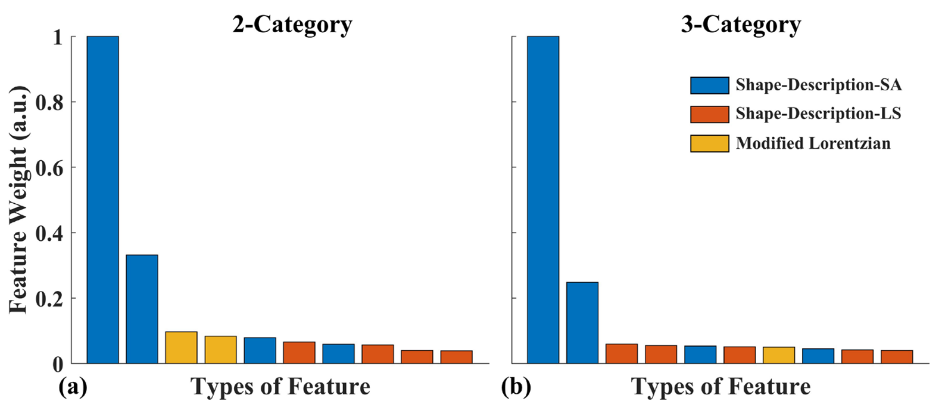

Figure 2.13. Top 10 normalized feature weights ranked by MRMR (minimum-redundancy-maximum-relevance) for (a) 2- and (b) 3-category woody breast classification, respectively.

Aside from the MRMR-based feature section, PCA (Jolliffe, 2002) was applied to reduce the full set of hand-crafted features into low-dimensional representations for sample classification. The discriminant model was sequentially trained using the first 5 to 155 PCs in a 5-PC increment for 2- and 3-category WB classification, respectively [Figure 2.14 (a)]. The first 15 PCs produced the best accuracy of 87.05% in the 2-category modeling, which is slightly higher by 0.44% ($P >$ 0.05) than that obtained from full-feature modeling (86.61%), and then the accuracy gradually declined to around 78% as more PCs were used. Similarly, in the 3-category modeling, the accuracy peaked at 68.63% with the first 20 PCs and then decreased as more PCs were modeled, showing comparable accuracy to the full-feature modeling (70.06%) while using a reduced set of features (or PCs).

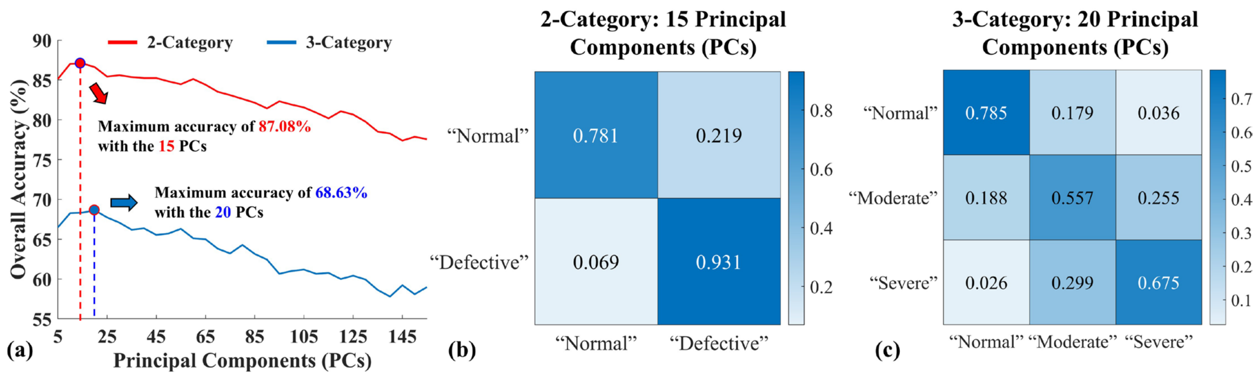

Figure 2.14. (a) Overall classification accuracies of using the first 5 to 155 principal components (PCs) in a 5-feature increment; row-wise confusion matrices (where row and columns correspond to actual and predicted labels) for (b) two and (c) three categories modeling based on the 15 and 20 PCs (best accuracy), respectively.

The corresponding confusion matrices for the 2- and 3-category classification are shown in Figure 2.14 (b) and (c). Likewise, the misclassification in 2-category modeling was primarily due to the "Normal" samples with a false negative rate of 21.9%, while a recognition accuracy of 93.1% was achieved for the "Defective" class. In 3-category modeling, the "Moderate" and "Severe" samples were relatively more difficult to differentiate, with misclassification rates of 25.5% and 29.9% between them, while 78.5% of the "Normal" samples were correctly classified, which are overall consistent with the results obtained using a smaller set of 140 features selected by MRMR [Figure 2.13 (c)].

2.6 Discussion

This chapter has demonstrated the feasibility of broadband LSI as a new approach to the assessment of WB conditions in broiler breast meat. Although direct comparisons with other imaging techniques in previous studies are challenging due to different samples and methodologies, the performance of LSI shown in this chapter is encouraging. Geronimo et al. (2019) reported

91.8% accuracy in classifying normal and WB-affected chicken samples using color images. Ekramirad et al. (2024) acquired optical coherence tomography images from normal and WB-affected chicken fillets and reported 95% classification accuracy. However, both studies were limited in their sample size, with 80 and 30 chicken fillets used for the 2-Category WB classification by Geronimo et al. (2019) and Ekramirad et al. (2024), respectively, as opposed to 242 samples in this study. The use of small sets of selected samples for modeling could result in an overestimation of model performance, which demands validations with more samples for reliable assessment. With a larger, more balanced set of sample data collected, an end-to-end deep-learning model trained from scratch could also be established for potentially improved WB assessment, which remains to be further investigated.

The current LSI platform only acquired broadband or panchromatic images, which can be upgraded into a multispectral mode by either using a multispectral camera or installing a filter device in front of the existing monochromatic camera, as done in Chapter 4. This would arguably result in additional spectral information, potentially translating into better performance in WB classification. However, the broadband LSI technique has better potential to be implemented for online WB detection of chicken meat at processing facilities. More dedicated efforts in both software and hardware are needed to move forward the technique beyond this proof-of-concept study toward practical application. In addition to the feature engineering-based approaches for WB assessment in this study, it is important to point out that the spatially-resolved scattering profiles extracted from scattering images can be utilized for inversely estimating absorption and scattering coefficients of meat samples based on light propagation models in biological tissues (Kienle et al., 1996; Bigio & Fantini, 2016), which provide quantitative insights into tissue optical properties and can inspire new approaches to poultry quality evaluation.

2.7 Conclusions

A broadband LSI technique was assembled and evaluated in this chapter for assessing WB conditions in broiler breast fillets. Normal and WB-affected samples showed differences in the characteristics of the shape of SA and LS areas as well as scattering profiles, providing the basis for utilizing scattering images to classify them into different WB categories. This chapter demonstrated that the hand-crafted features extracted from scattering images and profiles were useful for WB classification. The light attenuation levels that were used to define scattering areas for feature extraction affected model performance. The full set of 196 engineered features from both saturation and scattering areas of scattering images yielded overall classification accuracies of 86.61% and 70.06% for 2- and 3-category WB classification, respectively, outperforming the deep learning-based features (76.43% and 55.36%) by a significant margin of 10.18% and 14.7% ($P < 0.05$). Further improvements of 87.92% and 70.77% were achieved by modeling subsets of 40 and 140 features selected by MRMR for 2- and 3-category WB classification, respectively, while PCA produced comparable accuracies of 87.08% and 68.63% using the first 15 and 20 PCs. More efforts are needed to develop classification models based on an expanded set of chicken samples and implement the imaging technique in multispectral mode (Chapter 4) while pursuing real-time implementation for online detection.

CHAPTER 3: ASSESSMENT OF WOODY BREAST CONDITION IN BROILER BREAST FILLETS USING SINUSOIDAL ILLUMINATION REFLECTANCE IMAGING COUPLED WITH SURFACE PROFILOMETRY

3.1 Imaging System

A benchtop broadband SIRI system, as schematically shown in Figure 3.1, was assembled for poultry imaging. The system mainly consisted of a quartz tungsten halogen (QTH) light source (Newport Corporation, Irvine, CA, USA) connected with a power supply controller, a digital light projector (DLP) (DLi6500 Optics Bundle, DL*i*, Austin, TX, USA) that uses a digital micromirror device of 1920 × 1080 pixels for spatial light modulation, a monochromatic camera (Edge 4.2, PCO, Kelheim, Germany) with a resolution of 2048 × 2048 pixels, equipped with a 35 mm fixed focal length lens (Edmund Optics Inc., Barrington, NJ, USA), and a desktop computer. The light from the QTH lamp passed through a visible-near-infrared liquid light guide (Newport Corporation, Irvine, CA, USA) to the DLP for light pattern illumination onto broiler breast samples for imaging.

The DLP and camera were synchronized by a trigger cable to allow for simultaneous pattern projection and image acquisition. The camera was positioned perpendicularly downward at about 50 cm above the sample, with a pixel resolution of about 0.1 mm/pixel. The projector was set up at an angle of about 10° with respect to the camera and 40 cm from the sample, illuminating an area of about 25 cm × 15.5 cm. A pair of crossed linear polarizers were attached in front of the projector and camera lenses to reduce specular reflection from the sample surface. The SIRI system was operated in an enclosed dark chamber for sample illumination and image collection to avoid the interference of ambient light.

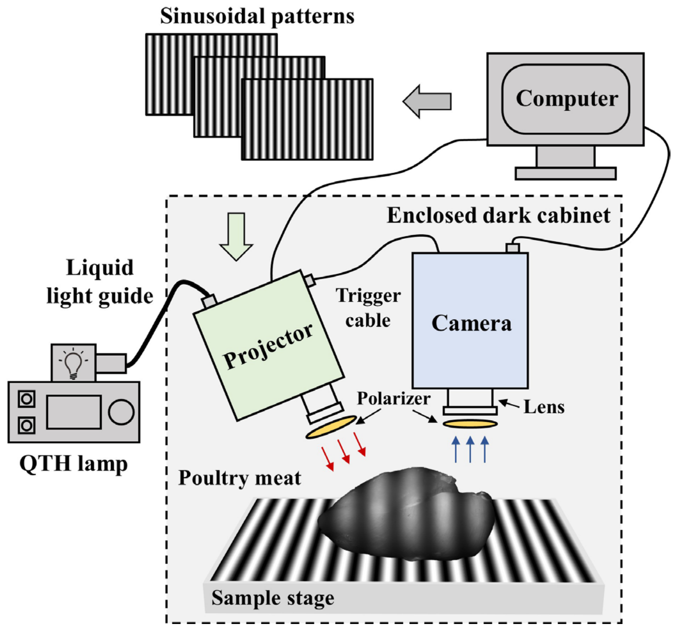

Figure 3.1. Schematic of a broadband SIRI system for assessing woody breast of broiler meat.

In SIRI, three phase-shifted sinusoidal patterns with phase offsets of 0, 2π/3, and 4π/3 at a given spatial frequency are normally used due to the ease of three-phase demodulation to retrieve intensity and phase images (Lu & Lu, 2019). In this chapter, images were acquired under the illumination of a sequence of three-phase-shifted patterns at eight different spatial frequencies of 0.015-0.150 cycles/mm. These spatial frequencies differ from those in our previous studies on white striping (WS) assessment of broiler meats (Olaniyi et al., 2023a, 2023b, 2024), because physical calibration of the illumination patterns was further considered in this study. These patterns were generated as 8-bit bitmaps in Matlab R2022R (The MathWorks Inc, Natick, MA, USA) and then loaded to the graphical interface software (LightCrafter 6500/9000 GUI, Texas Instruments, Dallas, Texas) of the projector for sample illumination. The same groups of samples were used in this study for all imaging (LSI and SIRI) and texture instrumental experiments (as well as in Chapter 4), with detailed descriptions provided in Chapter 2. The broiler samples were individually placed on a sample stage and imaged under consecutive switching of a set of 24 preloaded illumination patterns (24 = 3 phase-shifted patterns per spatial frequency × 8 spatial frequencies) triggered by the camera bundled software (camware v4.2, PCO, Kelheim, Germany) with an exposure time of 500 ms.

3.2 Image Processing

The acquired pattern images were first processed by a low-pass Gaussian filter of 3×3 pixels kernel size to suppress image noise. Then, as illustrated in Figure 3.2, the acquired three phase-shifted pattern images at each spatial frequency were demodulated into DC, AC, and phase images as follows:

$$I_{DC} = \frac{1}{3}(I_1 + I_2 + I_3) \tag{3.1}$$

$$I_{AC} = \frac{\sqrt{2}}{3}\sqrt{(I_1 - I_2)^2 + (I_1 - I_3)^2 + (I_2 - I_3)^2} \tag{3.2}$$

$$\varphi = \arctan\left(\frac{\sqrt{3}(I_1 - I_3)}{(2I_2 - I_1 - I_3)}\right) \tag{3.3}$$

where I_1, I_2, and I_3 are the reflectance pattern images acquired under the illustration of three phase-shifted patterns at the same spatial frequency, and the demodulation operations are performed on a pixel basis. The intensity images, DC and AC, characterize the optical properties of a sample (Lu & Lu, 2019; Lu & Cai, 2023), while the phase image depicts the surface geometry of the sample (Figure 3.2). Thereafter, histogram-based automatic thresholding (Lu & Lu, 2017) was adopted on the DC images to separate broiler meat samples from the background and further applied to the corresponding AC and phase images.

It is important to note the arctangent function Eq. (3.3) for phase retrieval results in phase values wrapped to the range of – π to π, with 2π discontinuities or jumps in the resultant map, which is referred to as the wrapped phase (Zhang, 2018b). Further phase unwrapping is needed to restore the wrapped phase to a continuous phase map (also known as the absolute phase). The relationship between the absolute phase (ϕ) and wrapped phase (φ) is provided as follows:

$$\phi = \varphi + 2\pi k \tag{3.4}$$

where k is the integer number to represent fringe orders of the wrapped phase, which remains to be determined using a phase unwrapping technique.

Among numerous absolute phase recovery techniques, the two-frequency method (Zhang, 2018b), which employs the phase information obtained at low frequency to unwrap the high-frequency phase, was adopted in this chapter given its high-resolution [or signal-noise-ratio (SNR)] and precision for absolute phase retrieval. The fringe order k can be uniquely determined using the following equation (Huntley & Saldner, 1993; Zhao et al., 1994):

$$k = \mathrm{Round}\left(\frac{(f_h / f_l)\phi_l - \varphi_h}{2\pi}\right) \tag{3.5}$$

where Round() is a function that returns the closest integer value, f_h and f_l represent the spatial frequency of high and low fringe patterns, respectively, and φ_h and ϕ_l are the wrapped and absolute phases at the same high and low spatial frequencies, respectively.

Here the spatial frequencies of 0.03 cycles/mm (low-frequency) and 0.15 cycles/mm (high-frequency) were used to retrieve the phase map. The ϕ_l was coarsely restored by comparing the wrapped phase with the estimated reference phase using the method proposed by Wang et al., (2023), which suffers from low SNR and resolution in the phase map due to the sparse fringe distribution at a lower frequency. According to Eq. (3.5), though, the low-frequency phase ϕ_l can be used to determine the fringe order k of the wrapped phase at high frequency. With the fringe order k obtained, the high-frequency absolute phase ϕ_h with improved measurement resolution and precision was calculated using Eq. (3.4). Thereafter, a phase-difference map was attained by subtracting the estimated reference map from the absolute phase ϕ_h, which depicts the topographic surface profiles of a sample due to the proportional relationship between the phase difference and surface height (Lu & Cai, 2023; Lu & Lu, 2018c). Finally, the resultant phase difference maps were subjected to a median filter with 5×5 pixels kernel size to reduce noise, before subsequent feature extraction and modeling.

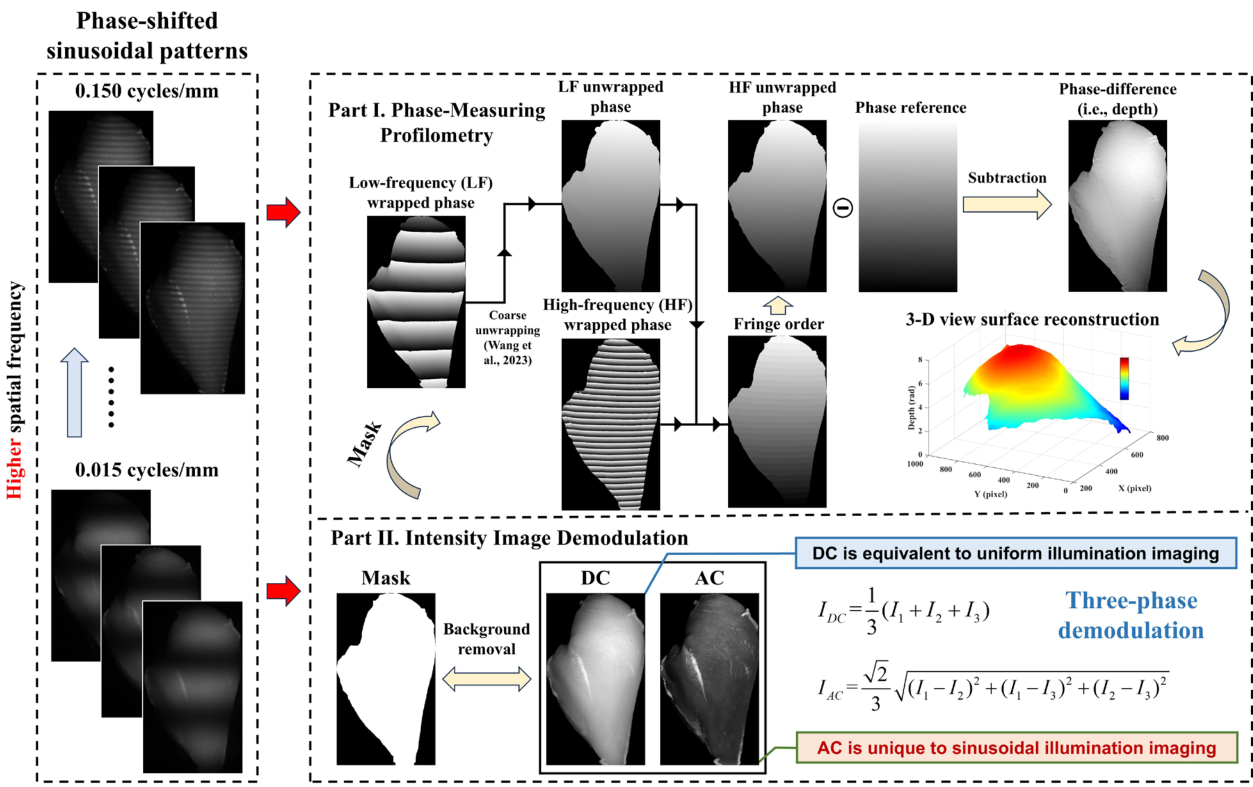

Figure 3.2. Image processing to obtain the phase-difference, direct component (DC), and amplitude component (AC) images using three phase-shifted patterned images at each spatial frequency.

3.3 Feature Analysis and Classification Modeling

The two sets of image data obtained, i.e., the phase images (Dataset I) and the intensity DC and AC images (Dataset II), were utilized separately for feature analysis and WB classification modeling, as shown in Figure 3.3. Previous studies have shown the superiority of using pre-trained deep-learning (DL) models over hand-crafted feature engineering in extracting textural features from intensity images for WS assessment of poultry meat (Olaniyi et al., 2023a, 2023b). Here, the pretrained image classification model, i.e., ResNeXt-101 (Xie et al., 2017), was used as a feature extractor for both phase and intensity images. As done for scattering images in Chapter 2 (Section 2.4), the output from the last convolutional layer of the model was taken as the features, which is a vector of 2048 features for each given input image. Although pretrained DL models were effective for extracting discriminative features from the demodulated intensity (DC and AC) images for assessing physical characteristics of meat samples (e.g., WS in poultry meat and beef marbling) (Olaniyi et al, 2023a, 2023b; Cai et al., 2024), the chance is that these models like ResNeXt-101 may not be well suited for representing the phase difference images in this study, because the phase difference images, which depict the surface geometry of samples, differ dramatically from DC or AC images or other types of natural scene images in the ImageNet database used for pre-training DL models.

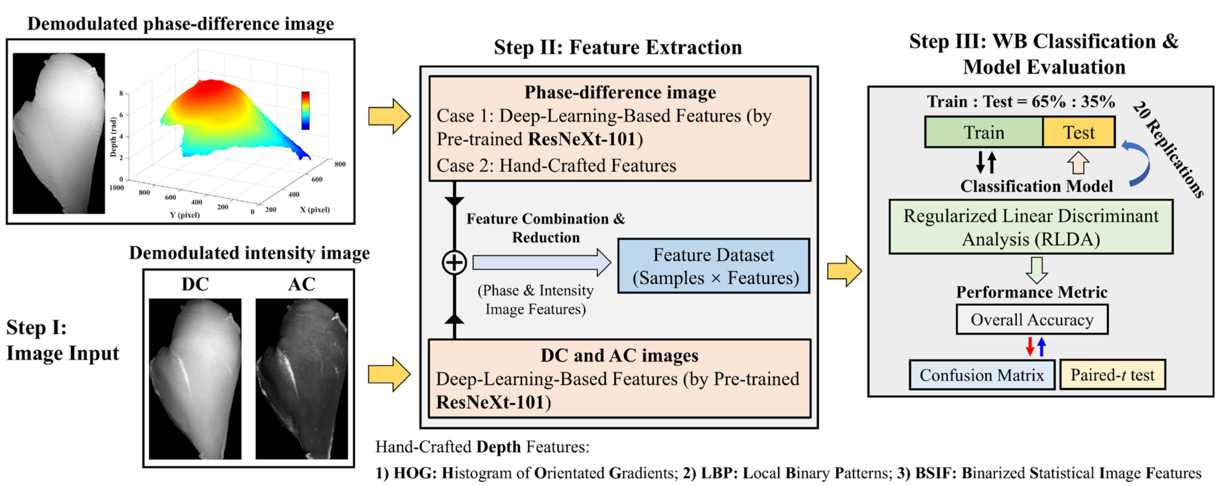

Figure 3.3. The procedures for classifying normal and WB-affected broiler meat samples using features extracted from intensity and phase-difference images.

Given the potential risk in using DL-based feature extraction for phase difference images, due attention was given to hand-crafted feature engineering, which may lead to more effective features than those obtained from the DL model, for capturing sample geometry. The histogram of gradient

(HOG) (Dalal & Triggs, 2005) and local binary patterns (LBP) (Ojala et al., 1996, 2002) are the image descriptors that capture local gradients and spatial structures (e.g., shape or contour) in images, which have been used to extract features from 3-D depth maps for human face/action recognition (Ali et al., 2018; Tatarenkov & Buchatsky, 2018; Chen et al., 2015). Inspired by LBP, binarized statistical image features (BSIF) provide meaningful representations of images by implementing filters learned using statistics of images for improved pattern classification performance (Kannala & Rahtu, 2012).

In this chapter, as indicated in Figure 3.3, all three types of local descriptors (HOG, LBP, and BSIF) were extracted from the phase difference images to build the set of hand-crafted features as opposed to the DL-based features for WB assessment. These features, which were extracted using an open-source Matlab Toolbox Balu (version 4.1) (Mery, 2011), included 1800 HOG, 59 LBP, and 128 BSIF. The HOG feature set was constructed using 20×10 spaced cells in horizontal and vertical directions with 9 histogram bins, resulting in 1800 features. The LBP features were calculated for 58 rotation-invariant uniform patterns and all non-uniform patterns defined in an 8-pixel neighborhood (Ojala et al., 2002). For the BSIF descriptor, the features were extracted with a filter size of 5×5 pixels and 7-bit length, which is the default setting of the Balu toolbox (Mery, 2011). Since both filter size and the length of the bit string affect the resultant feature set and downstream model performance (Kannala & Rahtu, 2012), the two parameters were empirically tuned in extracting features from phase-difference images for improved model performance by varying the filter size from 3 to 17 (in an increment of 2), followed by adjusting the bit length from 5 to 12 with the optimized filter size (see Section 3.4.2). The extracted hand-crafted features were concatenated in different combinations for model development and performance evaluation.

For each sample, the DL-based features were extracted from both phase-difference and intensity (DC and AC) images at different spatial frequencies, while the hand-crafted (HOG, LBP, and BSIF) features were only used on the phase-difference image. Classification models were built for WB assessment by using the phase-difference and intensity image features separately as well as their combination. As done in Chapter 2 (Section 2.4), the extracted feature dataset was randomly partitioned into training and test sets according to the ratio of 65% : 35%, and RLDA (Guo et al., 2007) was employed to build models for differentiating between normal and WB-affected samples. The two tunable hyperparameters of RLDA, including the regularization parameter γ ($0 < \gamma < 1$) and the shrinkage δ ($\delta > 0$), were optimized through grid search with 10-fold cross-validation on training data. To obtain a reliable estimate of model performance, a 20-repeated holdout validation was carried out for model training/testing, and the averaged accuracy over the 20 replications was calculated as the primary metric for performance evaluation.

Feature analysis and classification modeling were performed using the DL framework PyTorch (version 1.13.1) and the scikit-learn library (version 1.0.2) in Python (version 3.8.16) and the Balu Toolbox (Mery, 2011) in Matlab R2022R (The MathWorks Inc, Natick, WA, USA) on a desktop computer with an Intel® Core™ i9-10900x CPU (256 GB RAM) and an NVIDIA RTX A6000 GPU (with 48 GB RAM).

3.4 Results

3.4.1 Demodulated Images

Figure 3.4 shows example phase-difference images of normal and defective (affected by moderate and severe WB) chicken fillets. These images reflect the topographic surface profiles of samples. The defective broiler examples, particularly the ones affected by severe WB defects (third row, Figure 3.4), with the color bar ranging from blue to red representing surface geometry/height, show ridge-like bulges along the cranial to caudal region varying with the severity of WB, while the normal (no WB) samples presented with relatively flat and uniform shape profiles (first row). These surface profiles characterize the physical shape differences visually observed, as shown in Figure 2.2. Hence, the image (geometric) features that represent the sample surface profiles are likely to be effective for classifying normal and WB-affected samples.

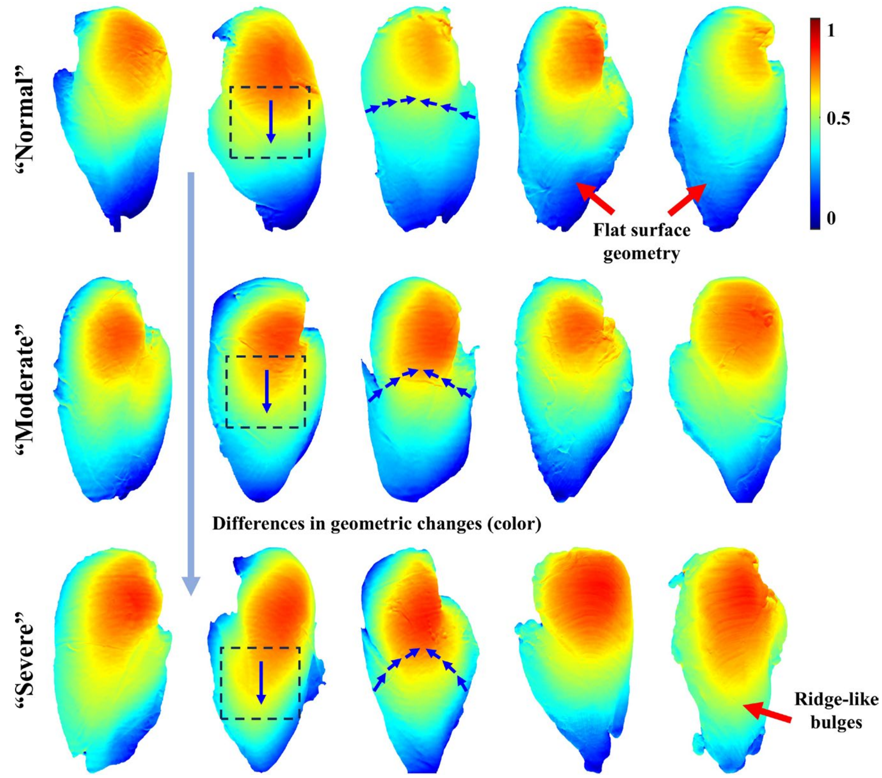

Figure 3.4. Examples of demodulated phase-difference (or phase-depth) images of normal and defective (affected by moderate and severe WB myopathies) broiler breast fillets.

Figure 3.5 shows examples of demodulated intensity (DC and AC) images of normal and WB-affected samples. Compared with DC, AC images vary with spatial frequency and appear to provide better visualization of textural characteristics (e.g., white striations) of samples, except that the intensity of AC images diminishes as the spatial frequency increases. This observation on intensity images is in agreement with previous poultry and beef imaging (Olaniyi et al., 2023a, 2023b, 2024; Cai et al., 2024). However, the intensity images reveal little information on the geometry of samples. It is reported that WS is sometimes co-occurrent with WB in broiler meat to a varying degree due to the interrelated histological changes in the affected muscles (Bowker et al., 2019; Aguirre et al., 2020). The co-occurrence of WS in the WB-affected samples could potentially contribute to differentiating between normal and defective samples in modeling textural features extracted from the intensity images. It should be noted that, in this study, most of the normal (WB-free) samples showed no incidence of WS defects, while only a small percentage (around 30% through visual inspection) of WB-affected samples (e.g., the last row example in Figure 3.5) were affected by WS defects.

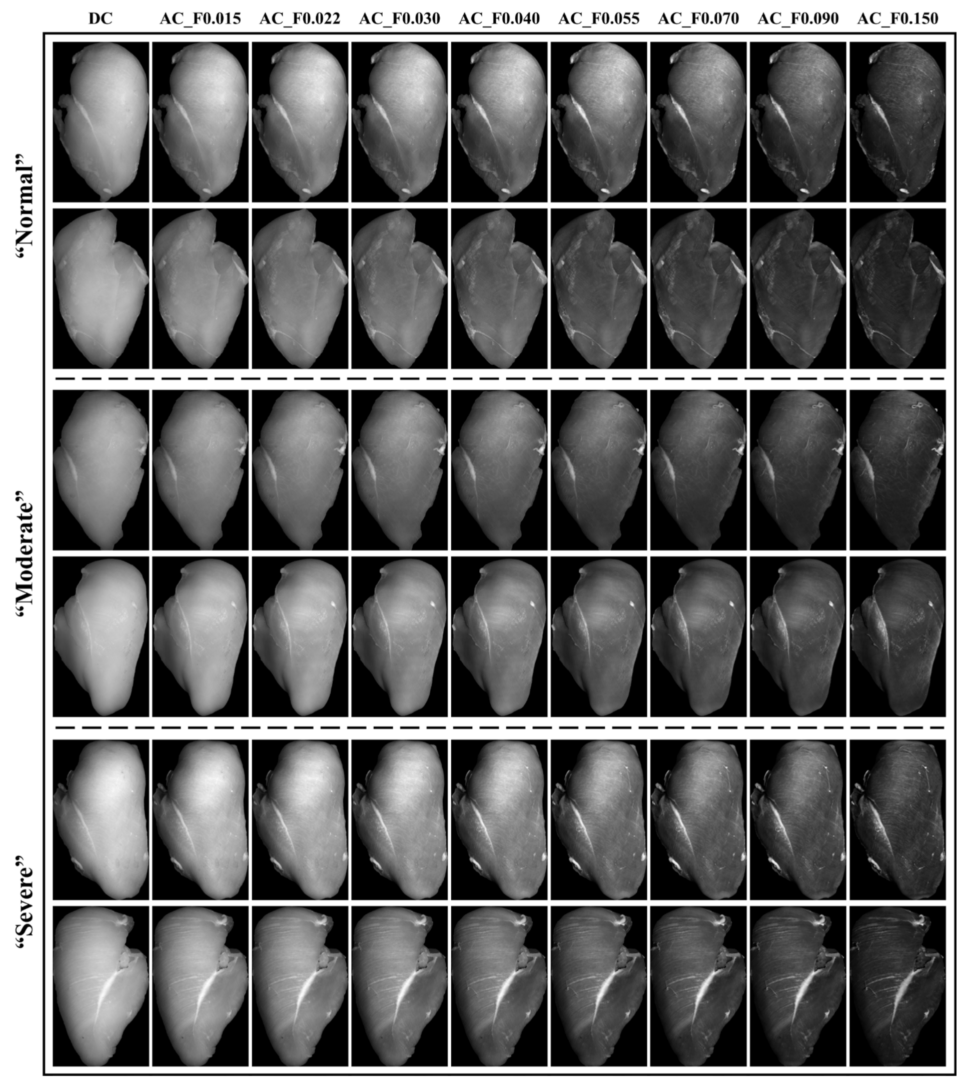

Figure 3.5. Examples of demodulated intensity images, i.e., direct component (DC) and amplitude component (AC), at the spatial frequencies of 0.015–0.15 cycles/mm (from left to right) for normal and WB-affected broiler breast samples.

3.4.2 Classification

The two types of features extracted from the phase-difference images, i.e., 1) DL-based and 2) hand-crafted geometric features, were used for building RLDA models for classifying broiler fillet samples into two and three WB categories. Figure 3.6 (a) shows the overall classification accuracy based on the DL-based features and different sets of hand-crafted feature sets. In the 2-category classification, the DL-based features yielded overall accuracy of 71.96%, while the hand-crafted features achieved better performance (given higher accuracy and smaller variations), with overall accuracies ranging from 82.62%-87.86%, representing significant improvements of 10.66%-15.90% ($P < 0.05$). Among the three types of hand-crafted features, LBP and BSIF outperformed HOG substantially, yielding the classification accuracy of 86.13% and 87.86%, respectively. Likewise, in the 3-category modeling, the hand-crafted features achieved consistently better classification accuracy (58.69%-71.49%) over the DL-based features (50.06%), and the best accuracy of 71.49% was obtained by BSIF and LBP-BSIF combined features, which generally agreed with the results in the 2-category modeling, except with overall lower accuracies. It is noted that the combination of hand-crafted features [1) LBP and BSIF combined and 2) HOG, LBP, and BSIF combined] produced mediocre improvements in both 2- and 3-category modeling scenarios, i.e., slightly lower/identical accuracy and no statistically significant differences ($P > 0.05$), confirming that BSIF were more effective than LBP and HOG for WB assessment.

The scattering plot based on the first two PCs of the BSIF features, as shown in Figure 3.6 (b), confirmed the separation between normal (blue marker) and WB-affected (green and yellow markers) broiler fillet samples; however, there was also an overlap observed between moderate and severe WB categories, resulting in less effective in differentiating between samples of these two WB categories and thus negatively impact the overall performance in 3-category WB classification (discussed below, Figures 3.9 and 3.10).

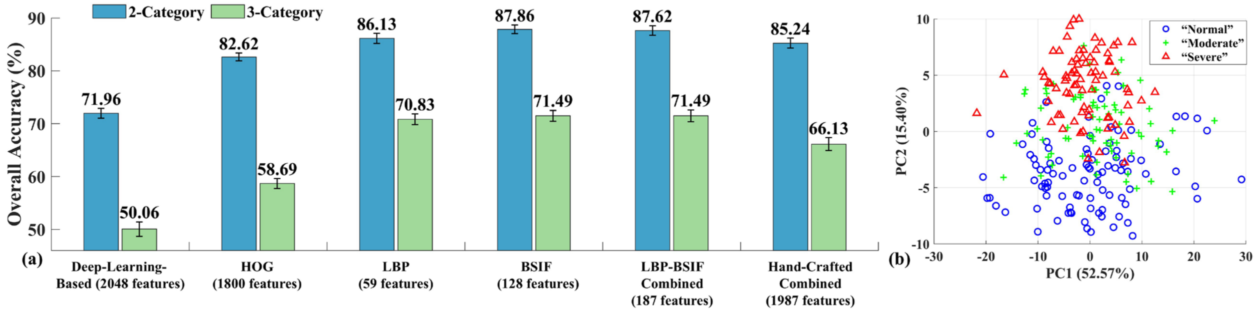

Figure 3.6. (a) Overall classification accuracies of deep-learning-based and hand-crafted features extracted from phase-difference images for two and three WB categories modeling; (b) scatter plot of the BSIF features in the space spanned by the first two principal components (PCs) for three WB categories of chicken fillet samples. HOG, LBP, and BSIF denote histograms of gradient, local binary pattern, and binarized statistical image features, respectively.

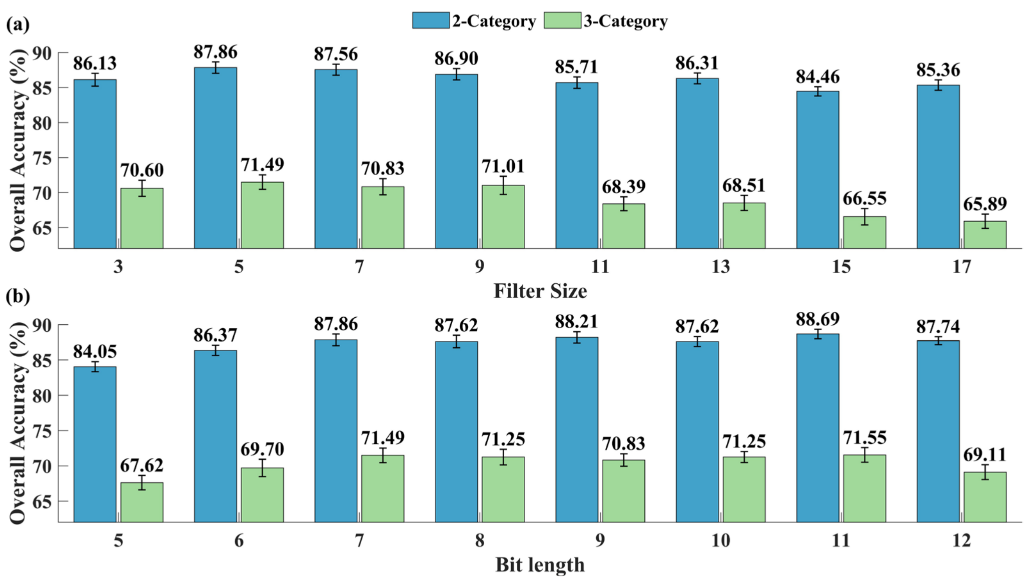

Figure 3.7. Overall classification accuracies by modeling binarized statistical image features (BSIF) extracted for different (a) filter sizes and (b) bit length.

Among the three types of hand-crafted features, the BSIF showed the most discriminative ability. To exploit BSIF for improved WB assessment, its two parameters, including the filter size and bit length (Kannala & Rahtu, 2012), were tuned to extract better feature sets from the phase-difference images. For the sake of optimization efficiency, instead of conducting an exhaustive grid search for the best parameter pair, the filter size was first tuned with the bit length set to default, and thereafter the bit length was tuned by applying the optimized filter size. Figure 3.7 shows the effect of varying the parameters on the classification accuracies. Overall, it seems the accuracy decreased with relatively larger filter sizes and increased with relatively larger bit lengths in both 2- and 3-category modeling scenarios. In first-round optimization, tuning the filter size to 5 × 5 pixels yielded the local highest accuracy of 87.86% and 71.49% in 2- and 3-category modeling [Figure 3.7 (a)], respectively, which are identical to those obtained by the default BSIF (Figure 3.6); further improved accuracies of 88.69% (2-category) and 71.55% (3-category) were then obtained with the bit length set to 11 [Figure 3.7 (b)]. The optimized BSIF (with 5 × 5 pixels filter size and 11 bit length) produced overall accuracies of 0.83% and 0.06% better than that achieved before optimization (see Figure 3.6), despite no statistically significant improvements ($P > 0.05$).

Figure 3.8 shows the overall classification accuracies using the intensity image (DC and AC) features and their combination with the hand-crafted features from the phase-difference images for classifying normal and WB-affected broiler fillet samples. The feature combination was done by concatenating the optimized BSIF features (5 × 5 pixels filter size and 11-bit length) with the features of AC images at individual spatial frequencies to produce the ensemble of AC-phase image features. In the 2-category classification, the DC images produced a baseline overall accuracy of 80.24%, while the AC images offered better accuracies of 81.43%-84.88%, and the highest accuracy of 84.88% was obtained at 0.055 cycles/mm, which is 4.64% higher than that obtained by DC ($P < 0.05$). Similar results were observed in 3-category modeling, where AC images remained superior over DC, yielding the highest improvement of 4.58% at both 0.055 and 0.150 cycles/mm (64.88%) than that obtained by DC (60.30%). The combined features of AC and phase difference images yielded significant improvements at all the spatial frequencies, with the overall classification accuracy ranging from 86.07%-87.74% and 70.00%-72.08% in 2- and 3-

category modeling, respectively, outperforming the AC image features used alone.

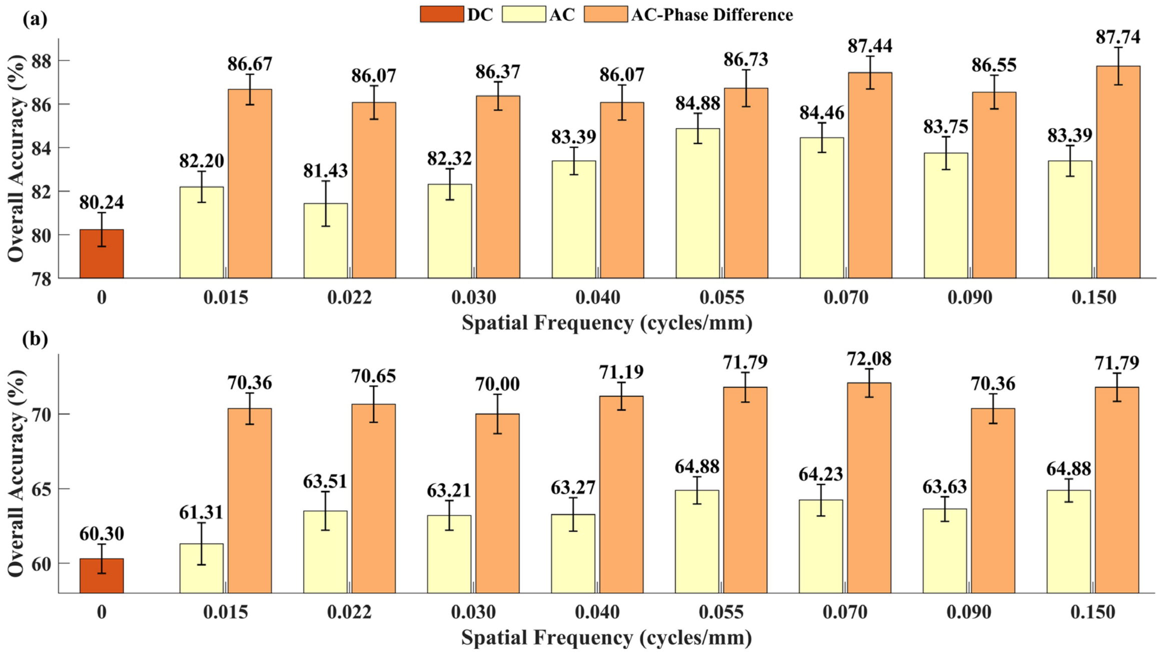

Figure 3.8. Comparison of overall accuracies for the intensity image [direct component (DC) and amplitude component (AC)] features and the combination of AC image features with the phase-difference image features in classifying broiler meat samples into (a) two and (b) three WB categories.

These results validated the positive effects of the geometric features from the phase-difference images for WB assessment. The best feature combination in 2-category modeling (with 87.74% accuracy at 0.150 cycles/mm) still fell behind the hand-crafted features, i.e., the optimized BSIF (88.69%), of the phase-difference images, with a small accuracy gap of 0.95% from that achieved by the latter, while in 3-category, slightly improved accuracies of 71.79% and 72.08% were obtained by concatenating the optimized set of BSIF with textural features from the AC images at 0.055, 0.070, or 0.150 cycles/mm. Despite higher accuracies (71.79% and 72.08%), the combined features showed no statistically significant improvements ($P > 0.05$) over that obtained by the optimized BSIF alone (71.55%), where the numerical difference in accuracy is primarily attributed to the randomness of modeling. These suggest that the phase image-derived geometric features contributed primarily to the success in classifying normal and WB-affected chicken meat samples while the AC image-derived textural features were less effective.

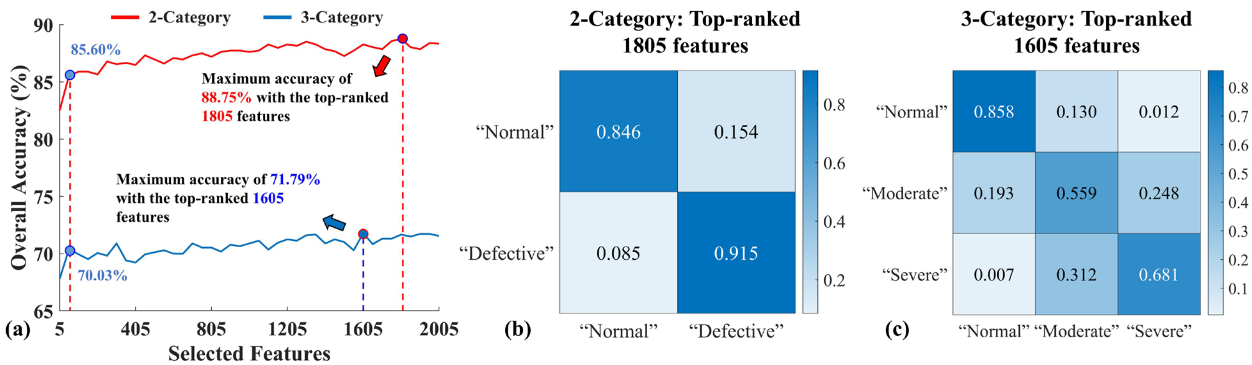

Figure 3.9. (a) Overall classification accuracies of using subsets of the most relevant hand-crafted scattering features ranked by the MRMR algorithm, ranging from 5 to 2005 in an increment of 50; row-wise confusion matrices (where row and columns correspond to actual and predicted labels) for (b) two and (c) three WB categories modeling based on the top-ranked 1805 and 1605 features (best accuracy), respectively. The confusion matrix was obtained by pooling and row-wise normalizing classification results in 20-repeated holdout validations.

As done in Chapter 2, two feature reduction methods, i.e., MRMR and PCA, were adopted to reduce model complexity and potentially improve classification accuracy. Considering the primarily positive effect of the phase-derived features, the best feature set, i.e., the optimized BSIF, of phase difference images was chosen as the feature base for dimensionality reduction in both 2- and 3-category modeling scenarios. Figure 3.9 (a) shows the overall accuracies for 2- and 3-category WB classification using the top 5 to 2005 features in a 50-feature increment, ranked by importance according to the MRMR algorithm (Ding & Peng, 2005). In 2-category modeling, the top-ranked 55 features yielded an overall classification accuracy of 85.60%, which is comparable to that obtained from full-feature modeling [88.69%, see Figure 3.7 (b)]. The accuracy fluctuated around 85%-88% and then peaked at 88.75% when the top-ranked 1805 features were used for modeling. In 3-category modeling, an overall accuracy of around 70% was achieved starting from the top 55 features, with the highest accuracy of 71.79% obtained using the top-ranked 1605 features. The selected features, i.e., 1805 and 1605 feature subsets, although were not effectively simplified by MRMR, produced slight improvement of 0.06% and 0.24% ($P > 0.05$) over those of the full-feature set for 2- and 3-category WB classification, respectively.

Figure 3.9 (b) and (c) show the corresponding confusion matrices for the classification results. In 2-category modeling, the misclassification was primarily due to the "Normal" class with a false negative rate of 15.4%, while 91.5% of the "Defective" samples were correctly classified. In 3-category modeling, the "Normal" samples were well differentiated from the WB-affected ones, particularly from those of the "Severe" class [with less than 2% misclassifications, Figure 3.9 (c)], obtaining an overall classification accuracy of 85.8%; however, distinguishing between the "Moderate" and "Severe" classes remained challenging, with misclassification rates of 31.2% and 24.8% between them. Further efforts are needed to improve the performance in differentiating between the "Moderate" and "Severe" samples.

PCA (Jolliffe, 2002) was further examined to reduce the full set of BSIF features into low-dimensional representations for WB classification. The RLDA model was trained using the first 5 to 155 principal components (PCs) in a 5-feature increment, and the overall classification accuracy on the test data is shown in Figure 3.10 (a). In the 2-category classification, the accuracy peaked at 89.29% using the first 30 PCs, and then slightly decreased as more PCs were modeled. Similarly, in the 3-category classification, the highest accuracy of 69.23% was achieved using the 20 PCs, after which the accuracy fluctuated and slightly declined. The corresponding confusion matrices for the classification results are shown in Figure 3.10 (b) and (c). Likewise, in 2-category modeling, the "Defective" samples were more accurately classified than the "Normal" samples (85.4%), achieving a recognition accuracy of 91.9% [Figure 3.10 (b)]. In 3-category modeling, the misclassification primarily occurred between the "Moderate" and "Severe" classes, with 50.7% and 65.5% of samples correctly classified, respectively, while 85.1% of normal samples were successfully differentiated from the WB-affected samples. Notably, an overall accuracy of above 95% was achieved for classifying between the "Normal" and "Severe" samples [1.7% and 1% misclassifications, Figure 3.10 (c)]. PCA produced comparable accuracies to those achieved using MRMR-selected features for modeling (Figure 3.9), while significantly reducing the feature dimensions (PCs), which helps improve model efficiency and minimize the risk of overfitting, making it more promising for online WB detection.

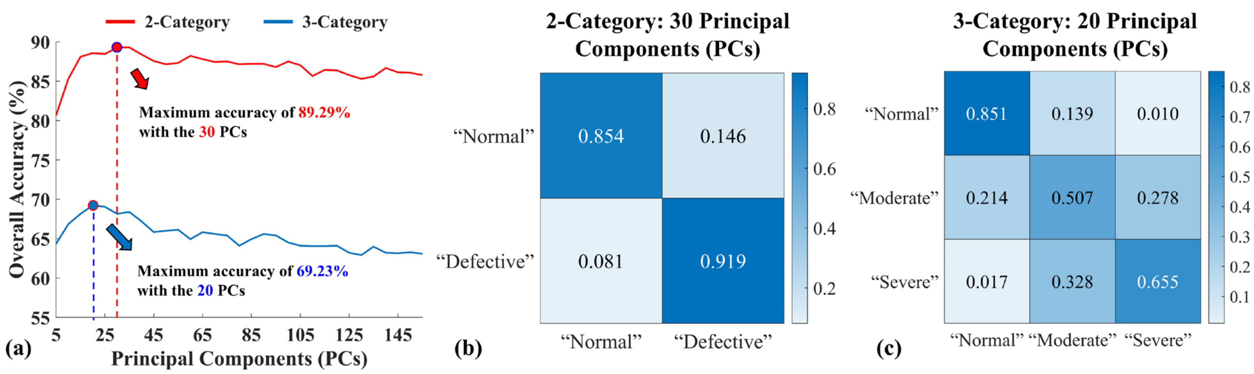

Figure 3.10. (a) Overall classification accuracies of using the first 5 to 155 principal components (PCs) in a 5-feature increment; row-wise confusion matrices (where row and columns correspond to actual and predicted labels) for (b) two and (c) three WB categories modeling based on the 30 and 20 PCs (best accuracy), respectively.

3.5 Discussion

This chapter presents a proof-of-concept validation of the applicability of broadband SIRI coupled with phase analysis for classifying broiler fillet samples into two and three categories according to WB conditions. The SIRI technique allows reconstruction of the surface topography of chicken samples, which is reflected in the retrieved phase-difference images, for enhanced WB assessment in comparison with using intensity images (DC and AC), which differs from 2-D computer vision techniques reported on poultry WB assessment (Geronimo et al., 2019; Caldas-Cueva et al., 2021; Yoon et al., 2022). It should be noted that the pipeline for feature engineering and model development outlined in this chapter has room for further optimization and improved

WB classification, although the BSIF feature extraction was locally optimized. Although noticeable accuracies of around 95% were reported for the 2-category WB classification in (Yoon et al., 2022; Ekramirad et al., 2024), these previous studies only examined a small collection of chicken samples (fewer than 50) and often lacked reliable repeated validations in their modeling pipeline, which could lead to an overestimate of classification performance.

Further research into SIRI will involve collecting an expanded, more balanced set of broiler samples to enhance model performance, especially to improve the accuracy of differentiating between moderate and severe WB-affected samples. Since the present SIRI acquires only broadband images, given the efficacy of spectral sensing for WB assessment (Wold et al., 2017, 2019, 2020; Pallerla et al., 2024), it is possible to enhance WB assessment by implementing SIRI in multi-/hyper-spectral mode. Notably, in addition to the phase analysis-based SIRI technique in this chapter, other 3-D imaging techniques such as time of flight and stereovision can also provide surface topography of poultry samples. It would be worthwhile to pursue a dedicated study on performance evaluation of 3-D imaging techniques for WB assessment of broiler meat, especially given the availability of cost-effective, consumer-grade depth cameras. The off-the-shelf depth cameras may not deliver high-precision 3-D maps but are compact standalone imagers that can be readily implemented for high-speed food quality detection (Xu et al., 2024). It is also important to point out that the SIRI technique can be applied to quantify and map optical properties (absorption and scattering) of poultry tissues using the computational methods developed in the spatial frequency domain imaging (Cuccia et al., 2009; Bigio & Fantini, 2016; Lu et al., 2020a), which would provide more insights into WB assessment of poultry meat.

Moving forward, the SIRI system of this chapter, which was only applied to stationary samples, has yet to be upgraded for real-time quality detection of moving samples, which is challenged by the lengthy acquisitions of multiple (three patterns/frames in this chapter) phase-shifted sinusoidal pattern images at a given spatial frequency. Single-shot image demodulation, which has been researched in the field of optical metrology and biomedical optics (Feng et al., 2019; Aguénounon et al., 2019), will be a viable solution to the implementation of real-time SIRI if intensity (DC and AC) and phase images can be retrieved from single-phase images with minimal artifacts. Recently, generative artificial intelligence has received considerable attention in image generation. These generative models (Liu et al., 2024; Zuo et al., 2024) have the potential to achieve single-frame image demodulation, facilitating the online implementation of SIRI.

3.6 Conclusions

This chapter presents an evaluation of a broadband SIRI system for assessing WB conditions in broiler breast fillets. The surface profiles of samples reconstructed using a phase demodulation and processing procedure captured the shape differences between normal and WB-affected chicken samples, while the demodulated intensity (DC and AC) images revealed only the surface texture characteristics of samples. An algorithm pipeline extracted different types of features from the phase difference images (depicting sample geometry) and the intensity images and built models for classifying normal and defective (affected by moderate and severe WB defects) broiler fillet samples. The hand-crafted features of the phase difference images were more effective for WB assessment than the textural features of either DC or AC images. Overall accuracies of 88.69% and 71.55% were achieved using the optimized set of BSIF from phase difference images for 2- and 3-category WB classification, respectively, representing improvements of 3.81%-8.45% and 6.67%-11.25% over the accuracy obtained by textural feature from DC and AC images. The ensemble of the optimized phase-derived features and the intensity image features yielded higher accuracies than using the features of intensity images alone, but still overall underperformed the phased-derived features, except for slight but insignificant improvements ($P > 0.05$) of 71.79% and 72.08% in 3-category modeling, implying that the sample geometry was more relevant than surface texture characteristics to WB assessment. Feature reduction that applied to the optimized phase-derived BSIF produced improvements of 89.29% (2-category) and 71.79% (3-category) by modeling 30 PCs and a subset of 1605 features selected by MRMR, respectively. This chapter has demonstrated the efficacy of broadband SIRI with surface profilometry for WB assessment in broiler breast meat.

CHAPTER 4: FEASIBILITY INVESTIGATION OF MULTISPECTRAL IMAGING FOR EVALUATION OF WOODY BREAST IN BROILER BREAST FILLETS

4.1 Multispectral Imaging

4.1.1 Introduction

Multispectral imaging captures image data at multiple, discrete wavelengths, enabling analysis of the properties of products or scenes through both spatial and spectral information. Given the non-invasive and versatile capabilities, multispectral imaging technology has received considerable attention in the agriculture and food fields over the past few decades (Qin et al., 2013). Most multispectral imaging systems share three hardware components, i.e., light source, wavelength dispersive device, and detector (Lu et al., 2017). A light source is to generate light, usually broadband light (as opposed to the laser that produces a narrow band of wavelengths), to illuminate samples. A wavelength dispersive device is used to disperse incident light into separate wavelengths and project the dispersed light onto an area-array detector (usually a digital camera) for data acquisition.

Different types of wavelength dispersive devices are available, enabling different spectral image acquisition approaches. There are three common types of wavelength dispersive devices, e.g., a filter wheel that contains multiple bandpass filters, imaging spectrographs, and electronically tunable filters (ETFs). Mounted in front of a monochromatic camera, a filter wheel enables acquiring spectral images sequentially by rotating the wheel, either manually or automatically, with different filters in place. This approach offers some flexibility in selecting bandpass filters of interest and can be a cost-effective way to implement multispectral imaging. It is generally limited to imaging at a small number of wavebands (basically 4~8) and inefficient in image acquisition especially when manual rotation is required. Imaging spectrographs use diffraction gratings (e.g., prism-grating-prism) for wavelength dispersion based on the fact that the direction of light propagation within is wavelength dependent (Qin et al., 2017), which is capable of providing high spectral resolutions and wide spectral ranges. They are generally used for line scanning measurements in hyper-spectral imaging systems.

ETFs are used for area scanning measurements; two major types of ETFs exist, including acousto-optic tunable filter (AOTF) and liquid-crystal tunable filter (LCTF) (Abdlaty et al., 2018). The AOTF is a diffraction-based device that works as an electronically tunable bandpass filter based on light-sound interactions in an anisotropic crystal (Stratis et al., 2001). Its wavelength selection is controlled by varying the frequency of acoustic waves applied to the crystal. The LCTF, on the other hand, is a birefringent-based device that uses phase retardance (delay) between ordinary and extraordinary light passing through a liquid crystal to isolate a single wavelength from the incident broadband light. Both AOTF and LCTF are capable of rapid wavelength selection while preserving imaging integrity in terms of spatial and spectral resolutions (Abdlaty et al., 2018); yet the LCTF is more compact and flexible in design, making it easy to integrate into various optical imaging systems. Over the past few decades, therefore, LCTF-based multispectral imaging systems have been assembled and utilized in medical diagnosis (Abdulhalim et al., 2007; Vega et al., 2024) and further extended to applications in food quality inspection (Peng & Lu, 2006b, 2006c; Lu & Lu, 2018a; Lohumi et al., 2021).

4.1.2 Multispectral LSI and SIRI Systems

This chapter was built on Chapters 2 and 3, where broadband LSI and SIRI were evaluated, to build multispectral LSI and SIRI systems and achieve potentially enhanced assessment of WB conditions in broiler breast fillets. Both the earlier broadband LSI and SIRI systems were upgraded into multispectral mode by installing an LCFT (VariSpec, Cambridge Research and Instrumentation, Inc., Woburn, MA, USA) that operate in the wavelength range of 650-1,000 nm, in front of the existing monochromatic camera, as schematically shown in Figure 4.1. The LCTF in each stage consists of a pair of parallel polarizers with a liquid crystal layer in between (Beeckman et al., 2009; Abuleil & Abdulhalim, 2016). In the SIRI system, therefore, the LCTF, in addition to working as an electronically tunable bandpass filter, also plays a role in suppressing specular reflections from poultry samples in conjunction with a separate linear polarizer mounted in front of the projector (acting as a pair of crossed linear polarizers) (Lu & Lu, 2018a).

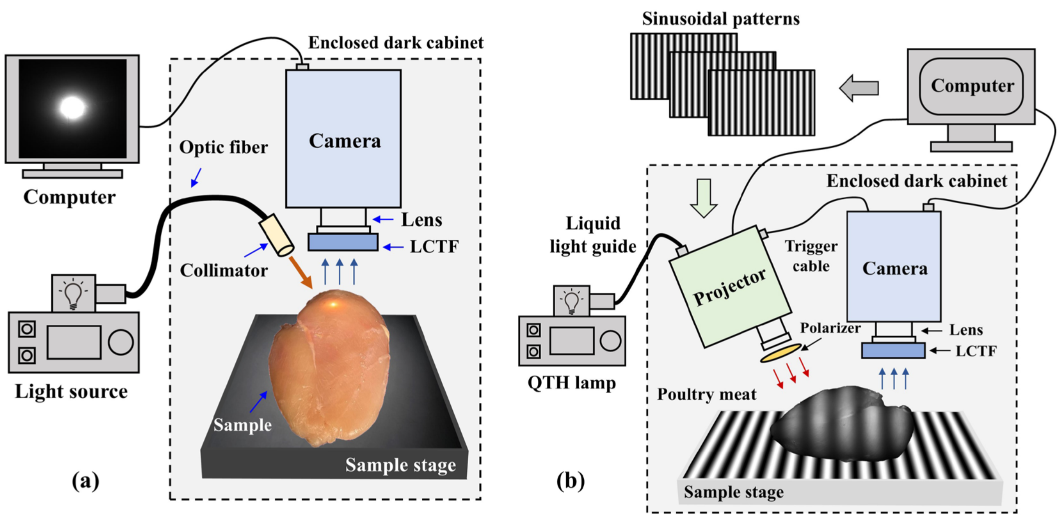

Figure 4.1. Schematic of multispectral LSI (a) and SIRI (b) systems.

The same groups of samples as in Chapters 2 and 3 were used for multispectral LSI and SIRI experiments. Except for the addition of the LCTF, all other hardware configurations remained the same as the corresponding broadband imaging described in Sections 2.3 and 3.1. The graphical interface software (i.e., Varispec) developed with Matlab programming was used to control the LCTF for selecting wavebands of interest. To ensure adequate image quality, the camera exposure times were set to 1,500 ms and 2,000 ms for multispectral LSI and SIRI systems, respectively. For LSI, a total of 36 spectral scattering images were acquired by adjusting the LCTF in the region of 650-1,000 nm in 10 increments. Given the relatively lengthy acquisition process in multispectral SIRI, which required about 1 minute to capture images (i.e., 24 patterned images) for each sample at a given waveband, a larger waveband increment of 15 nm was implemented in tuning the LCTF for image collection, resulting in a total of 24 spectral images for each meat sample in the multispectral SIRI system.

4.2 Classification Modeling for Multispectral LSI

Figure 4.2 shows the modeling pipeline for classifying broiler breast samples using multispectral scattering images. Given the validated efficacy in Chapter 2, the same types of hand-crafted features, including 1) NIA, 2) MLD, and 3) Shape-Description features, continued to be used in this chapter for feature extraction from scattering images at individual wavebands. As done in Chapters 2 and 3, the extracted feature data was randomly split into training and test sets according to the ratio of 65% : 35%, and a RLDA model was then built to classify broiler breast samples based on WB conditions. The scattering images were modeled separately for each waveband, ranging from 650 nm to 1,000 nm in increments of 10 nm, to identify the optimal wavebands or spectral ranges for WB assessment in broiler meat samples. The extracted features from individual wavebands were concatenated together to enhance the classification performance. Likewise, a holdout validation with 20 replications was performed to provide a reliable estimate of model performance across all wavelengths.

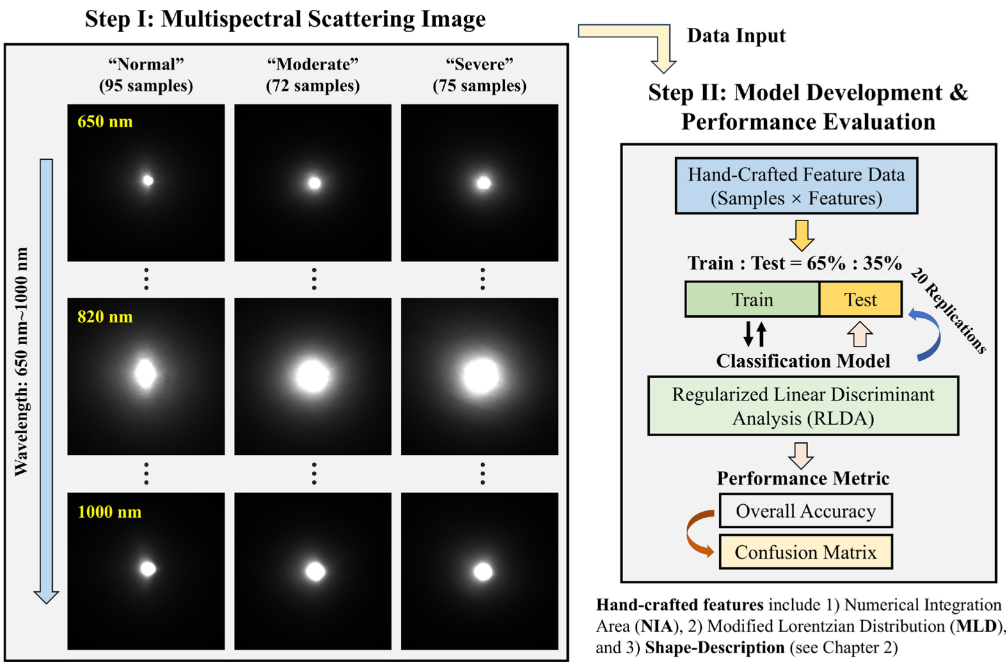

Figure 4.2. The procedures of using the multispectral scattering images for woody breast assessment of broiler breast meat.

4.2.1 Results

Figure 4.3 (a) shows the mean spectra of scattering images delimited by a light attenuation level of 10% (excluding the saturation areas) for broiler meat samples of three WB categories. Since the scattering images are spatially dependent, reference target-based calibration, which is commonly used in multi-/hyper-spectral imaging to correct for non-uniform instrument responses at different wavebands (Lu et al., 2020b), was not applied in this study. Despite the uncorrected spectra, the differences among the three WB categories still existed in their spectral curves [Figure 4.3 (a)]. The WB-affected samples ("Moderate" and "Severe") appeared to have higher reflectance in the wavelength range of 650-1,000 nm than the "Normal (no WB)" samples. As shown in Figure 4.3 (b), the differences among the three WB categories can also be visualized in the scatter plot using the first two PCs of their mean spectra, where PC1 and PC2 account for 92.06% and 7.30% of the total variance, respectively. However, it appeared to be difficult to distinguish between the "Moderate" and "Severe" samples due to the substantial overlap between them [Figure 4.3 (b)], which is consistent with the observations in Chapters 2 and 3.

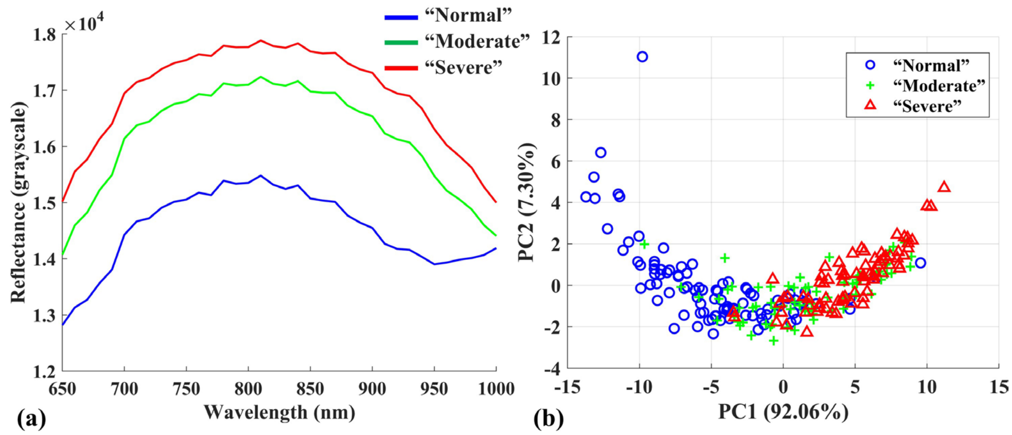

Figure 4.3. (a) Mean spectra (uncorrected) of scattering images delimited by a light attenuation level of 10% (excluding the saturation areas) for broiler meat samples of three WB categories; (b) scatter plot in the space spanned by the first two principal components (PCs) for three WB categories of broiler meat samples.

To further validate the potential of spectral information for WB assessment, quantitative modeling was performed by taking the mean spectra of broiler samples (at 36 wavebands) as input for RLDA modeling, obtaining overall accuracies of 82.98% and 63.63% for 2- and 3-category WB classification, respectively. These results indicate the positive effects of using spectral information on WB assessment in broiler fillets.

Figure 4.4 shows the overall accuracies achieved with different sets of hand-crafted features at individual wavebands (from 650 nm to 1,000 nm) for 2-category (red) and 3-category (blue) WB classification of broiler meat samples, respectively. For the NIA features, higher classification accuracy was observed in the near-infrared (NIR) range compared to the visible (VIS) range, with the maximum accuracies of 81.67% and 63.93% for 2- and 3-category classification achieved at 970 nm and 1,000 nm, respectively [Figure 4.4 (a)]. Similarly, the MLD features produced better classification performance in the NIR region, yielding the highest accuracies of 83.63% (2-category) and 63.15% (3-category) at 930 nm and 940 nm, respectively [Figure 4.4 (b)]. The shape-description features consistently outperformed the NIA and MLD in classifying broiler meat samples, which is in agreement with the findings in Chapter 2. The maximum accuracies of 85.36% (2-category) and 68.15% (3-category) were achieved by shape-description features at 730 nm and 860 nm, respectively [Figure 4.4 (c)].

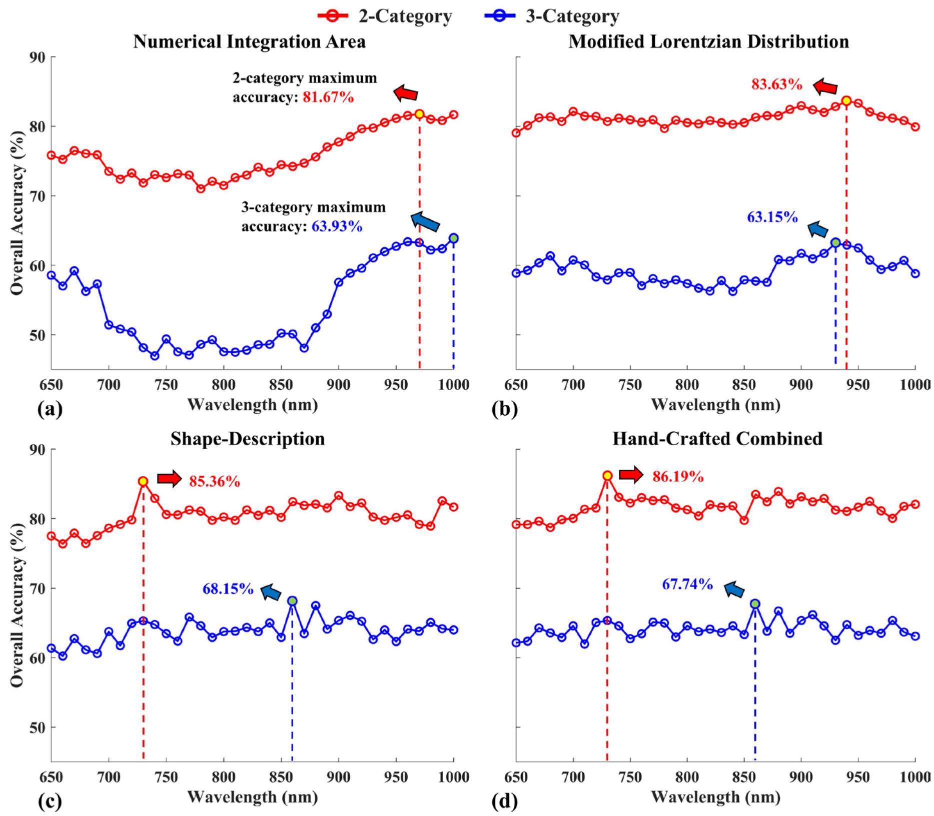

Figure 4.4. Comparisons of overall accuracies for the hand-crafted features extracted from scattering images at individual wavebands between 650 nm and 1,000 nm in increments of 10 nm, for two- and three-category WB classification, including (a) numerical integration area (NIA), (b) modified Lorentzian distribution (MLD), (c) shape-description, and (d) the combined set of features, respectively.

Unlike the NIA and MLD, both of which produced better performance in the NIA region, the shape-description features yielded inconsistent classification performance between 2- and 3-category modeling, as well as relatively large variations across the wavelength, making it difficult to identify a specific waveband or spectral range that most effective for WB classification in broiler meat. These three types of hand-crafted features at individual wavebands were then concatenated together for model classification. An improved accuracy of 86.19% was obtained in 2-category modeling, while a slightly lower accuracy of 67.74% ($P > 0.05$), compared to the accuracy of 68.15% by the shape-description features, was obtained for 3-category classification. Compared to the classification results achieved by the broadband LSI system in Chapter 2, where the best overall accuracies (without feature reduction) were 86.61% and 70.06% for 2- and 3-category classification, respectively, the result of 86.19% (2-category) and 68.15% (3-category) obtained in this chapter under multispectral scattering imaging was slightly worse. This is likely because the above modeling analysis was carried out separately for each individual waveband. Concatenating hand-crafted scattering image features across multiple wavebands could potentially improve the performance of WB classification.

Figure 4.5 shows the overall accuracies of using the combined sets of hand-crafted features across multiple wavelengths (up to 36) for WB classification. The hand-crafted features from individual wavebands were firstly ranked by classification accuracy [Figure 4.4 (d)] and incrementally combined from 2 to 36 wavebands to assess the effect of feature combination across multiple wavelengths on WB classification. As the number of wavelengths increased, overall, the classification accuracy improved progressively at first, reaching a peak with a certain number of combined wavelengths, and then declined slightly as more wavelengths were combined for modeling. The highest 2-category classification accuracy of 87.20% was achieved when features from the top-ranked 10 wavebands were combined. Similarly, the best performance for 3-category modeling was obtained by combining features from the top 16 wavebands, resulting in an overall accuracy of 70.48%. Slight improvements in accuracy ($P > 0.05$) were achieved through concatenating hand-crafted features at different wavebands over the best accuracies of 86.61% (2-category) and 70.06% (3-category) by the broadband LSI in Chapter 2. The improvement was primarily driven by the hand-crafted features extracted from images in the VIS region, indicating that the spectral-based scattering imaging is beneficial for WB assessment. More dedicated studies are needed to further improve the performance of WB assessment in broiler breast meat.

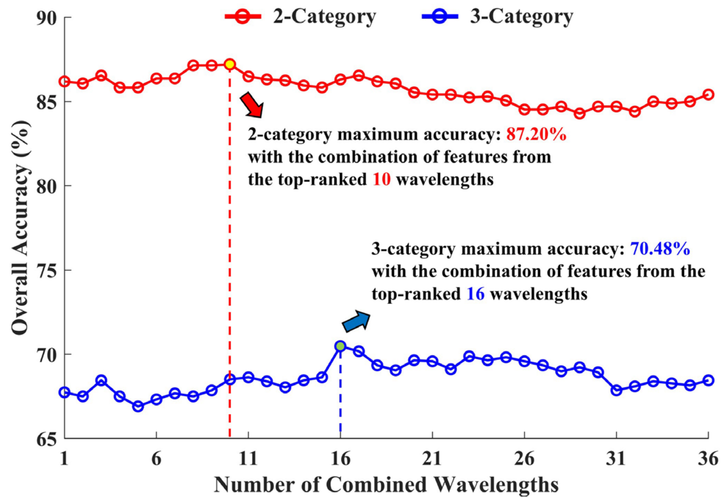

Figure 4.5. Distributions of overall accuracies of the combined hand-crafted features across multiple wavelengths (up to 36) for 2- and 3-category WB classification.

4.2.2 Discussion

Among the hand-crafted features for WB assessment, the shape-description features, while achieving higher accuracy, showed inconsistency between 2- and 3-category classification, as well as relatively large fluctuations in classification accuracy across the wavelengths. These variations is probably associated with the use of the LCTF in multispectral LSI system. The LCTF adopted in this study is a Lyot-based electronically tunable filter, with each stage consisting of a pair of parallel polarizers and a liquid crystal layer in between (Yang et al., 2010; Beeckman et al., 2009), as schematically shown in Figure 4.6. The linear polarizer is commonly used to confine the light field to a single plane along the direction of propagation, ensuring that light with a consistent polarization orientation passes through (Figure 4.7). However, the linear polarizer-based LCTF could lead to variations in the scattering images of broiler meat samples as the orientation of the LCTF/built-in polarizer changes, resulting in the inconsistency in shape characteristics of both the saturation area (SA) and light scattering (LS) area.

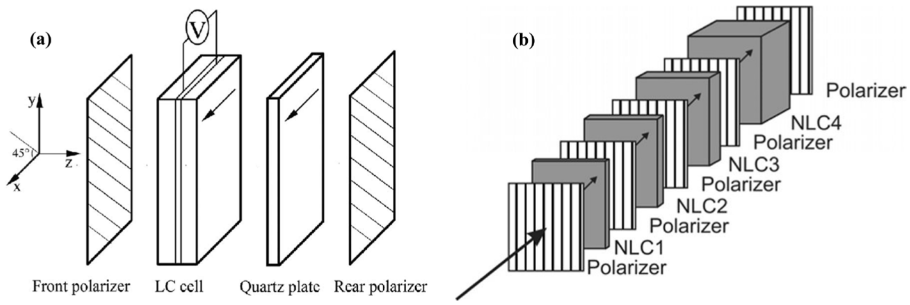

Figure 4.6. (a) Single stage of a Lyot LCTF that consists of a pair of parallel polarizers with a liquid crystal layer in between; (b) configuration of the Lyot LCTF (only shows four stages). Figures (a) and (b) are adapted from Yang et al. (2010) and Beeckman et al. (2009).

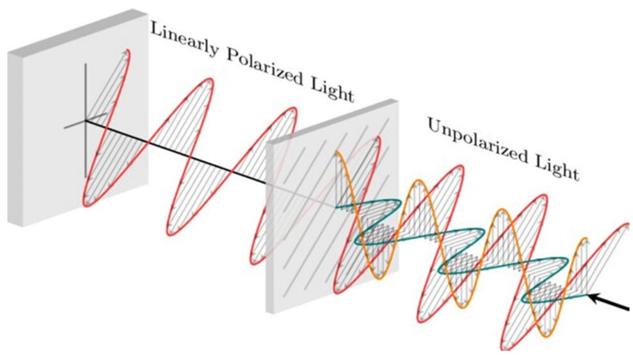

Figure 4.7. Schematic illustration of linear polarization. Figure is adapted from Blanchon et al. (2021).

To ascertain the hypothesized effect of polarizer orientation, scattering images of broiler meat samples were captured at different polarization directions, as shown in Figure 4.8. A polarization camera with on-chip polarizing filters in four different directions (LUCID, TRI050S1-PC, Richmond, Canada), i.e., 0°, 45°, 90°, and 135°, was used to replace the sCMOS-based camera (Edge 4.2, PCO, Kelheim, Germany) in the broadband imaging systems (Chapters 2 and 3) for polarization imaging tests. These findings indicate that using polarization-independent filtering devices, such as filter wheels, may be better suited than the LCTF for implementing multispectral LSI for WB assessment in broiler breast meat. Further efforts are needed to optimize the imaging setup of the current multispectral LSI system to achieve more accurate and reliable classification performance. Additionally, quantitative analysis to estimate optical absorption and scattering coefficients of chicken meat samples could provide more insights into WB assessment.

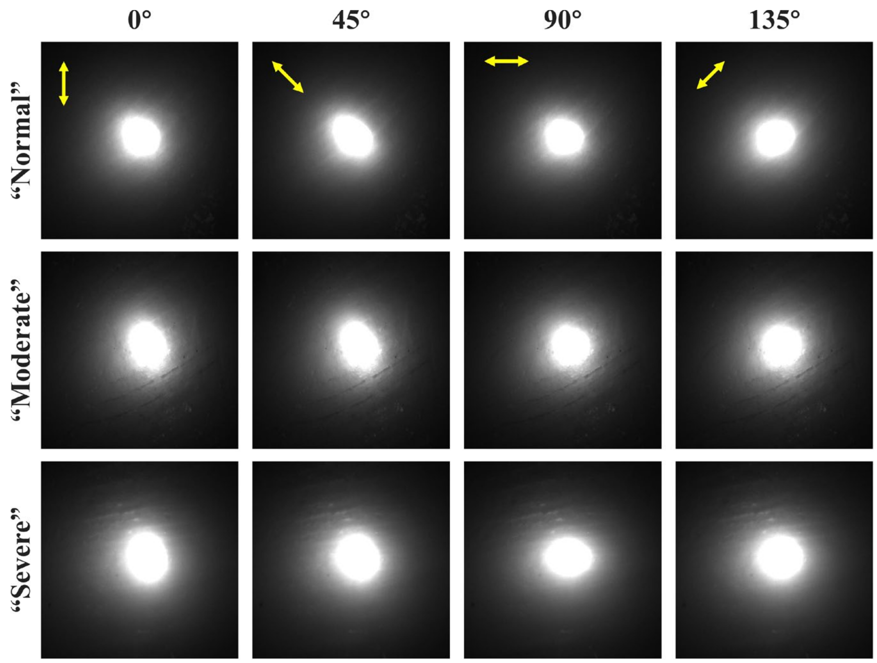

Figure 4.8. Examples of scattering images of normal and WB-affected (moderate and severe) broiler breast samples captured at four different polarization directions (0°, 45°, 90°, and 135°).

4.3 Classification Modeling for Multispectral SIRI

Chapter 3 has demonstrated the efficacy of broadband SIRI with surface profilometry for WB assessment in broiler breast meat. The phase-derived geometric features contributed more to the success in classifying broiler samples of different WB conditions, then features from the AC image. Multispectral imaging enables capturing image data across multiple different wavelengths. By selecting proper wavelengths or spectral ranges, it is possible to acquire images that enhance the characterization of textural features of broiler meat samples (e.g., white striping) and thereby the performance of subsequent modeling tasks. In this section, multispectral SIRI was evaluated to achieve potential improvements in the assessment of WB conditions in broiler meat samples. For each spatial frequency, a total of 24 spectral images were acquired by adjusting the LCTF in the region of 650-1,000 nm in 15 increments. The potential effect of textural features on WB assessment was explored using the newly developed multispectral SIRI system.

Figure 4.9 shows the procedures for classifying broiler breast samples using multispectral SIRI images. A pretrained ResNeXt-101 model was used for extracting features from the intensity images of DC and AC at individual wavelengths, respectively. Different from the intensity images that varied with the wavelengths, the phase image-derived surface profiles of samples were almost the same at all wavelengths. Hence, phase difference images were only required to be retrieved form SIRI pattern images at a single specific waveband for subsequent analysis and modeling. Binarized statistical image features (BSIF), which were the best hand-crafted feature set for WB assessment by broadband SIRI as validated in Chapter 3, were extracted from the phase difference images as compared with the textural features from intensity images across all wavelengths. Similarly, the feature data was randomly partitioned into training and test sets according to the ratio of 65% : 35%, and the RLDA was utilized to classify broiler breast samples into different categories according to their WB conditions. A holdout validation with 20 replications was carried out for performance evaluation across all wavelengths.

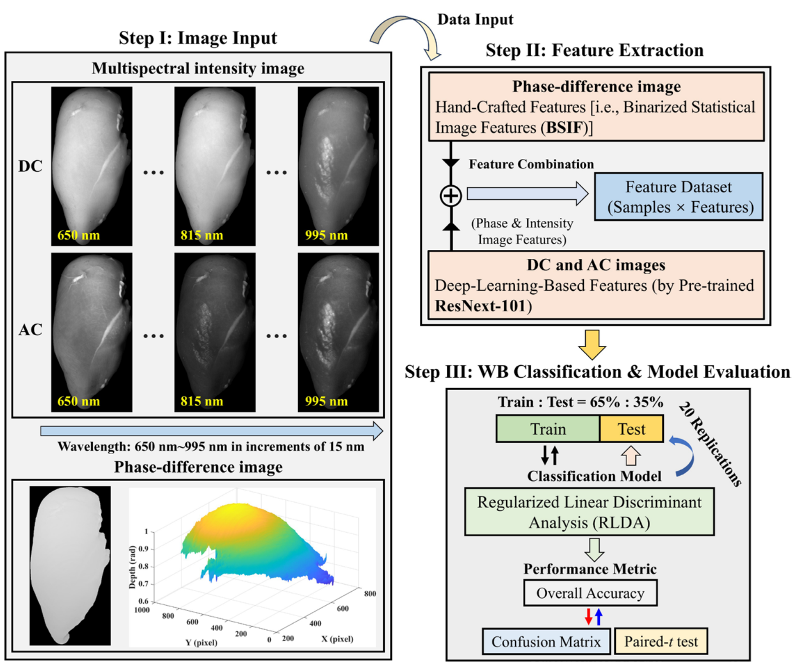

Figure 4.9. The procedures of classifying normal and WB-affected (moderate and severe) broiler meat samples based on the multispectral SIRI images.

4.3.1 Results

Given a 3-D multispectral datacube, mean spectra were extracted for each broiler meat sample by averaging the spectra of all pixels within the corresponding region of interest (sample mask). The corrected spectrum (i.e., relative reflectance) was then obtained by dividing the mean spectrum of each sample by that of the reference (white and dark) (Lu et al., 2020b). In the multispectral implementation of SIRI, two sets of spectral images, i.e., DC and AC, were obtained from the demodulation using phase-shifted pattern images at different spatial frequencies (Chapter 3). In this section, the demodulated intensity (DC and AC) images were used separately at each spatial frequency, thus allowing for extracting the spectral features of broiler meat samples at nine different spatial frequencies as used in Chapter 3.

Figure 4.10 (a) shows the corrected mean spectra of broiler meat samples of three WB categories extracted from DC images. The differences among WB categories were minimal based on the spectral curves. Substantial overlaps were also observed in the scatter plot of broiler samples [Figure 4.10 (b)], suggesting that these samples are not readily distinguishable through unsupervised approaches. Further, RLDA models were built for quantitative evaluation of classification performance. The corrected mean spectra of broiler samples at nine spatial frequencies were used separately as the input for discriminant modeling, with the results shown in Figure 4.11. Overall, these spectral features showed limited performance in classifying broiler samples, with relatively lower accuracies across all spatial frequencies than those achieved using broadband image features in Chapter 3. The maximum accuracies of 81.55% (2-category) and 62.8% (3-category) were attained at 0 and 0.150 cycles/mm, respectively. The results suggest spectral features were less effective than textural or depth features (Chapter 3) for WB assessment. However, it should be noted that the classification performance may vary with different processing and modeling approaches and could potentially be improved with optimized modeling.

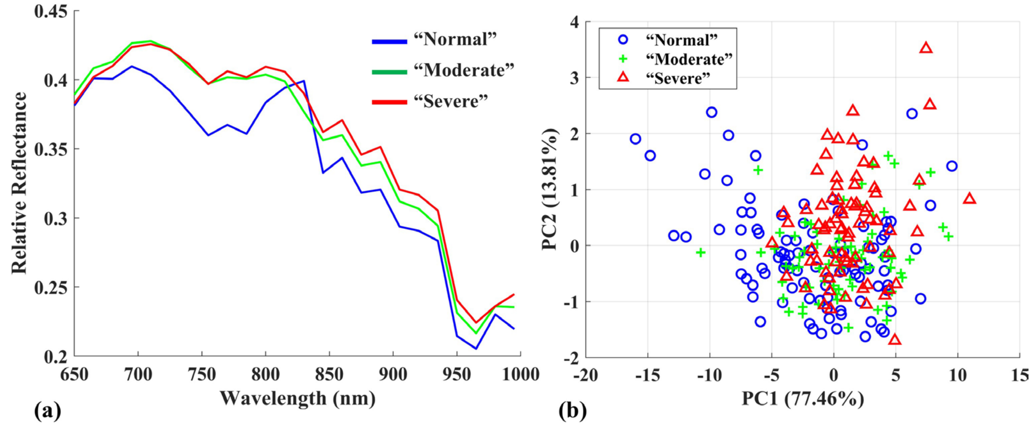

Figure 4.10. (a) Mean spectra (corrected) of broiler meat samples of three WB categories extracted from DC images; (b) scatter plot in the space spanned by the first two principal components (PCs) for three WB categories of broiler meat samples.

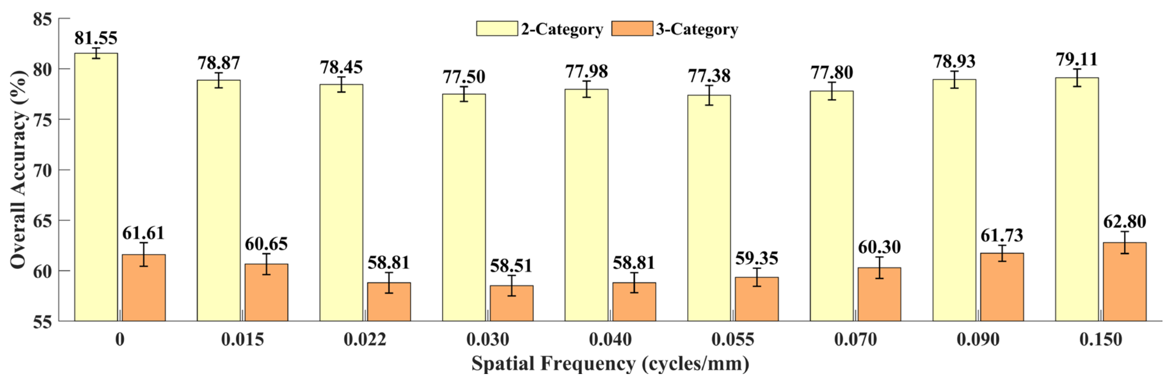

Figure 4.11. Overall accuracies of using mean spectra at different spatial frequencies (DC and AC) for two and three WB categories classification.

A further investigation was performed to utilize textural features extracted from images at individual wavebands for WB classification. Figures 4.12 shows the overall classification accuracies of textural features extracted from demodulated intensity images at different spatial frequencies across a wavelength range of 650–1,000 nm in increments of 10 nm. The classification performance varied across the spectral range, with overall higher and more stable accuracies achieved in the VIS wavebands compared to the NIR range. This is likely because textural features on the sample surface (e.g., WS) that are relevant to WB assessment were more effectively captured in the VIS region, thereby positively contributing to the classification modeling. On the other hand, in terms of spatial frequency, better accuracies were generally achieved at higher spatial frequencies in the range of 0-0.150 cycles/mm, which tend to resolve the characteristics of superficial meat tissues. Overall, these findings are in agreement with those in Chapter 3.

For the 2-category classification [Figure 4.12 (a)], the highest accuracy of 86.61% was achieved at a waveband of 755 nm and a spatial frequency of 0.150 cycles/mm, while for the 3-category classification [Figure 4.12 (b)], the maximum accuracy reached 65.06% at 770 nm and 0.090 cycles/mm. Given the consistently better performance observed in the 700-800 nm range, the 755 nm waveband was empirically chosen for obtaining phase difference images of broiler meat samples. The best phase-derived BSIF features (5 × 5 pixels filter size and 11 bit length, as validated in Chapter 3) were applied to the resultant phase difference images for feature extraction. Overall accuracies of 89.17% and 72.92% were achieved using the best set of BSIF from phase difference images for 2- and 3-category WB classification, respectively, representing improvements of 2.56% and 7.86% ($P < 0.05$) over the best accuracy obtained by textural features of AC images (Figures 4.12).

To further validate the effects of intensity image features on WB classification, the feature combination was done by concatenating the BSIF features with the features of AC images that produced the highest classification accuracy (Figures 4.12), resulting in a slightly lower accuracies of 89.11% and 71.37% for 2- and 3-category WB classification, respectively. Still, the ensemble of the phase-derived BSIF features and the intensity image features yielded higher accuracies than using the features of intensity images but underperformed the phased-derived features, implying that the sample geometry was more relevant than texture characteristics to WB assessment, despite enhanced surface textures by the multispectral SIRI.

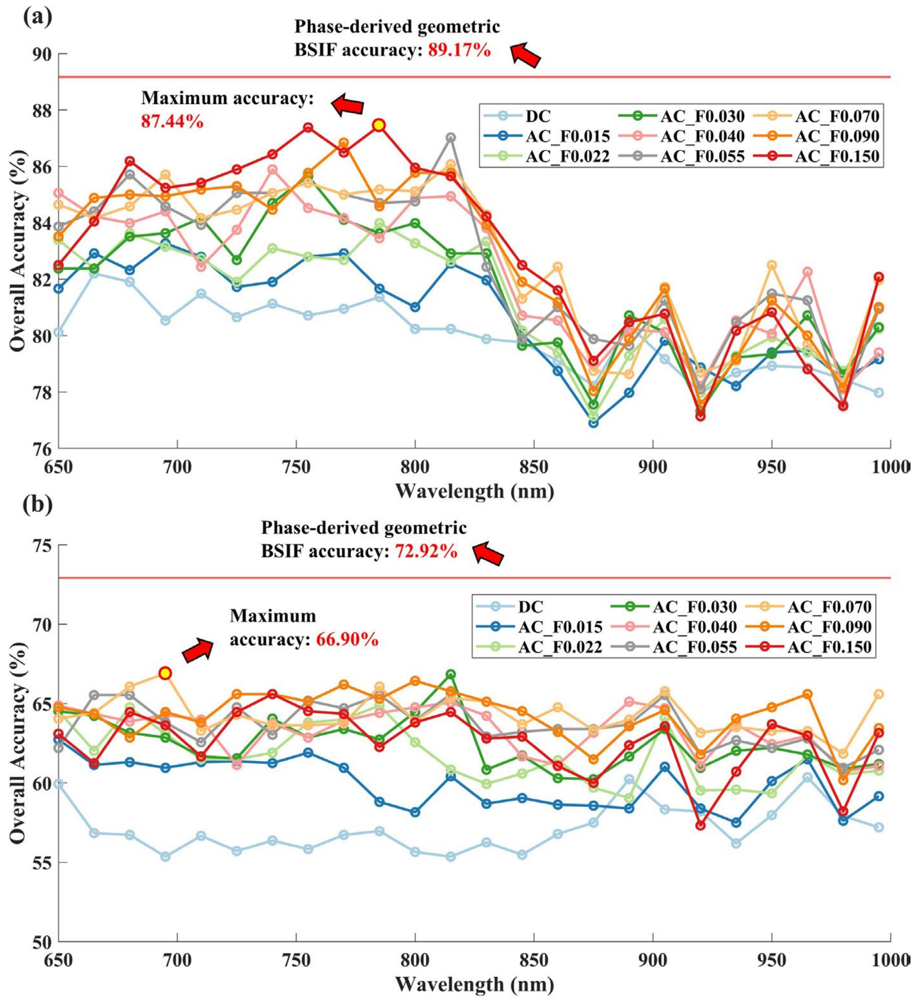

Figure 4.12. Comparisons of overall accuracies for the textural features extracted from demodulated intensity images at different spatial frequencies in the waveband range of 650-1,000 nm in increments of 10 nm for (a) two- and (b) three-category WB classification.

4.3.2 Discussion

This section presents an evaluation of the applicability of multispectral SIRI for classifying broiler meat samples according to WB conditions. Consistent with the conclusion in Chapter 3, the phase image-derived geometric features were more effective for WB assessment than textural features from either DC or AC images across the entire wavelength range of 650 to 1,000 nm in 10 nm increments. In this regarding, further research can be beneficial by evaluating other 3-D imaging techniques, e.g., time of flight (ToF) and stereovision, for WB assessment of broiler meat, especially considering the prevalence of cost-effective, consumer-grade depth cameras. In addition, although texture feature analysis based on intensity images was less effective for WB assessment, it is useful for assessing WS conditions in broiler meat (Olaniyi et al., 2023a, 2023b). Hence, it would be also worthwhile to pursue a dedicated study on the performance evaluation of SIRI for detecting the co-occurrent myopathies (e.g., WS and WB combined) in broiler meats, utilizing textural and shape features that specifically contribute to WS and WB detection, respectively. With SIRI, more insights into WB assessment can be gained by quantitatively estimating the optical properties (i.e., absorption and scattering) of chicken meat tissues (Cuccia et al., 2009; Bigio & Fantini, 2016; Lu et al., 2020a).

CHAPTER 5: DISCUSSION AND CONCLUSION

This study explored the potential of two emerging optical imaging techniques, i.e., LSI and SIRI, for assessing WB conditions in broiler breast fillets. The experimental results from the broadband LSI and SIRI in Chapters 2 and 3 provided initial insights into the texture/structural and shape characteristics of broiler meats associated with WB myopathy. For LSI, the differences between normal and WB-affected broiler samples were revealed in the characteristics of the shape of SA and LS areas as well as scattering profiles. The full set of 196 hand-crafted features extracted from scattering images achieved overall accuracies of 86.61% and 70.06% for 2- and 3-category WB classification, respectively, outperforming the DL-based features that yielded accuracies of 76.43% and 55.36%, with significant improvements of 10.18% and 14.7% ($P < 0.05$). SIRI, another emerging imaging technique examined in this study, which is capable of depth-resolved characterization and 3-D sample topography of samples, was evaluated for its effectiveness in WB defect detection as an alternative to conventional uniform illumination-based imaging. The phase-derived surface profiles of samples captured the shape (geometry) differences between normal and WB-affected chicken samples, while the demodulated intensity (DC and AC) images revealed only the surface texture characteristics of samples. The geometric features of phase difference images were more effective for WB assessment than the textural features of intensity images (i.e., DC and AC). Overall accuracies of 88.69% and 71.55% were achieved using the optimized set of BSIF from phase difference images for 2- and 3-category WB classification, respectively, representing improvements of 3.81%-8.45% and 6.67%-11.25% over the accuracy obtained by textural feature from DC and AC images.

Furthermore, multispectral LSI and SIRI systems were assembled by installing an LCTF in front of the monochromatic camera. Chapter 4 presents a preliminary investigation to evaluate the feasibility of multispectral LSI and SIRI for detecting WB conditions in broiler meat. For the multispectral LSI, slight improvements of 87.20% (2-category) and 70.48% (3-category) were obtained through concatenating hand-crafted features at multiple wavebands over the best accuracies (without feature reduction) of 86.61% and 70.06% by the broadband LSI in Chapter 2. However, the presence of linear polarizers in the LCTF caused variations in the scattering images of broiler meat samples depending on the LCTF's orientation, resulting in inconsistencies in the shape characteristics of both the SA and LS areas. This issue may be addressed by implementing multispectral imaging using a filter wheel-based wavelength-tunable device replacing the LCTF or directly a multispectral camera, for more accurate and reliable WB classification, On the other hand, multispectral SIRI produced the best classification accuracies of 89.17% and 72.92% using the optimized set of BSIF from phase difference images for 2- and 3-category WB classification, respectively. The ensemble of the phase-derived BSIF features and the intensity image features yielded higher accuracies than using the features of intensity images but still underperformed the phased-derived features, implying that the sample geometry was more relevant than surface texture characteristics to WB assessment.

It is also important to point out that, compared to 3-category classification, the 2-category classification is more practically meaningful for the time being, considering that at current poultry facilities identified WB-affected meat is generally discarded without resorting to further value-added processing, which otherwise would demand grading and sorting chicken fillets into 3 or more categories. The development of further processing techniques for the remediation or utilization of WB-affected meat is a research subject (Williams, 2024). The performance of WB classification in this study demonstrated encouraging results for 2-category modeling, achieving an accuracy of about 88% in differentiating normal and WB-affected samples, although the 3-

category modeling was less satisfactory, with an overall accuracy of around 71%.

Additionally, accounting for variations among three sample batches collected on different dates (Batch 1: 10/20/2023, Batch 2: 01/04/2024, and Batch 3: 05/09/2024) in this study, model performance may vary if training and testing are done batchwise, compared to polling combined batches for modeling as done in Chapters 2-4. Hence, further classification models were built using the first two batches for training (167 samples) and the remaining batch (75 samples) for testing to validate the generalization of the proposed methods for WB classification. Compared to the results achieved when all three batches of samples were mixed and then partitioned for training and testing, substantially lower accuracies were observed here with the first two batches of samples used for model training and the last batch for testing (Table 5.1), representing significant decreases of 6%-9% and 10%-16% (P < 0.05) for 2- and 3-category classification, respectively. The performance deterioration indicates the differences among sample batches, which have a negative impact on WB classification. Including more representative samples with greater variation for model training is expected to achieve more reliable classification results. To develop robust models, domain generalization techniques are also worth researching.

Table 5.1 Comparison of accuracies for 2- and 3-category WB classification using the first two batches of samples for model training and the last batch for testing.

Mode	Technology	2-Category Classification	3-Category Classification
Broadband	LSI	79.31%	59.77%
	SIRI	78.16%	60.92%
Multispectral	LSI	81.61%	55.17%
	SIRI	82.76%	60.92%

Despite methods developed in this study, there is a continuing need to expand the scope and depth of current research for a better understanding of WB myopathy in broiler fillet meats. Further efforts are needed to explore LSI and SIRI in hyperspectral mode, which will offers more abundant spectral information for tissue characterization and may lead to better differentiation among WB conditions in broiler meat. It is also important to point out that both LSI and SIRI can be utilized for quantifying optical properties (i.e., absorption and scattering) of meat tissues based on the modeling of light propagation in biological materials (Kienle et al., 1996; Cuccia et al., 2009), providing more insights into WB assessment of broiler meat. However, either hyperspectral-based imaging or optical property measurement would be limited to research purposes due to their relatively lengthy data acquisition and computational complexity (Lu et al., 2020a). In contrast, the broadband imaging shows better potential to be implemented for online WB detection of broiler meat at processing facilities. Additionally, the rapid developments in artificial intelligence over the past decade open opportunities for facilitating online WB detection, e.g., using deep generative models for potential single-frame image demodulation in SIRI, which warrants future work.

BIBLIOGRAPHY

Abdulhalim, I., Moses, R., & Sharon, R. (2007). Biomedical optical applications of liquid crystal devices. Acta Physica Polonica A, 112(5), 715-722.

Abuleil, M., & Abdulhalim, I. (2016). Narrowband multispectral liquid crystal tunable filter. Optics Letters, 41(9), 1957-1960.

Abdlaty, R., Sahli, S., Hayward, J., & Fang, Q. (2018). Hyperspectral imaging: comparison of acousto-optic and liquid crystal tunable filters. In Medical Imaging 2018: Physics of Medical Imaging, Vol. 10573, pp. 700-708. SPIE.

Aguénounon, E., Dadouche, F., Uhring, W., Giux, S. (2019). Single snapshot of optical properties image quality improvement using anisotropic two-dimensional windows filtering. Journal of Biomedical Optics 24(7), 071611.

Aguirre, M. E., Leyva-Jimenez, H., Travis, R., Lee, J. T., Athrey, G., & Alvarado, C. Z. (2020). Evaluation of growth production factors as predictors of the incidence and severity of white striping and woody breast in broiler chickens. Poultry science, 99(7), 3723-3732.

Ali, H. H., Moftah, H. M., & Youssif, A. A. (2018). Depth-based human activity recognition: A comparative perspective study on feature extraction. Future Computing and Informatics Journal, 3(1), 51-67.

Barbut, S. (2019). Recent myopathies in broiler's breast meat fillets. World's Poultry Science Journal, 75(4), 559-582.

Barbut, S., Mitchell, R., Hall, P., Bacon, C., Bailey, R., Owens, C. M., & Petracci, M. (2024). Myopathies in broilers: supply chain approach to provide solutions to challenges related to raising fast growing birds. Poultry Science, 103801.

Beeckman, J., Hui, T., Vanbrabant, P. J., Zmijan, R., & Neyts, K. (2009). Polarization selective wavelength tunable filter. Molecular Crystals and Liquid Crystals, 502(1), 19-28.

Bigio, I.R., Fantini, S. (2016). Quantitative Biomedical Optics: Theory, Methods, and Applications. Cambridge University Press.

Birth, G. S. (1978). The light scattering properties of foods. Journal of Food Science, 43(3), 916-925.

Birth, G. S., Davis, C. E., & Townsend, W. E. (1978). The scatter coefficient as a measure of pork quality. Journal of Animal Science, 46(3), 639-645.

Blanchon, M. (2021). Polarization based urban scenes understanding. Doctoral dissertation, Université Bourgogne Franche-Comté.

Bowker, B., Zhuang, H., Yoon, S. C., Tasoniero, G., & Lawrence, K. (2019). Relationships between attributes of woody breast and white striping myopathies in commercially processed broiler breast meat. Journal of Applied Poultry Research, 28(2), 490-496.

Bowker, B., & Zhuang, H. (2019). Detection of razor shear force differences in broiler breast meat due to the woody breast condition depends on measurement technique and meat state. Poultry Science, 98(11), 6170-6176.

Cai, J., Lu, Y., Olaniyi, E., Wang, S., Dahlgren, C., Devost-Burnett, D., & Dinh, T. (2024). Beef marbling assessment by structured-illumination reflectance imaging with deep learning. Journal of Food Engineering, 369, 111936.

Caldas-Cueva, J. P., Mauromoustakos, A., Sun, X., & Owens, C. M. (2021). Use of image analysis to identify woody breast characteristics in 8-week-old broiler carcasses. Poultry Science, 100(4), 100890.

Caldas-Cueva, J. P., & Owens, C. M. (2020). A review on the woody breast condition, detection methods, and product utilization in the contemporary poultry industry. Journal of Animal Science, 98(8), skaa207.

Cho, Y. J., & Han, Y. J. (1999). Nondestructive characterization of apple firmness by quantitation of laser scatter. Journal of texture studies, 30(6), 625-638.

Che, S., Wang, C., Iverson, M., Varga, C., Barbut, S., Bienzle, D., & Susta, L. (2022). Characteristics of broiler chicken breast myopathies (spaghetti meat, woody breast, white striping) in Ontario, Canada. Poultry Science, 101(4), 101747.

Chen, C., Jafari, R., & Kehtarnavaz, N. (2015). Action recognition from depth sequences using depth motion maps-based local binary patterns. In 2015 IEEE winter conference on applications of computer vision, pp. 1092-1099.

Cluff, K., Konda Naganathan, G., Subbiah, J., Lu, R., Calkins, C. R., & Samal, A. (2008). Optical scattering in beef steak to predict tenderness using hyperspectral imaging in the VIS-NIR region. Sensing and Instrumentation for Food Quality and Safety, 2, 189-196.

Cluff, K., Naganathan, G. K., Subbiah, J., Samal, A., & Calkins, C. R. (2013). Optical scattering with hyperspectral imaging to classify longissimus dorsi muscle based on beef tenderness using multivariate modeling. Meat Science, 95(1), 42-50.

Cuccia, D. J., Bevilacqua, F., Durkin, A. J., Ayers, F. R., & Tromberg, B. J. (2009). Quantitation and mapping of tissue optical properties using modulated imaging. Journal of biomedical optics, 14(2), 024012-024012.

da Silva, D. C. F., de Arruda, A. M. V., & Gonçalves, A. A. (2017). Quality characteristics of broiler chicken meat from free-range and industrial poultry system for the consumers. Journal of Food Science and Technology, 54, 1818-1826.

Dalal, N., & Triggs, B. (2005). Histograms of oriented gradients for human detection. In 2005 IEEE computer society conference on computer vision and pattern recognition (CVPR'05), Vol. 1, pp. 886-893.

Dalgaard, L. B., Rasmussen, M. K., Bertram, H. C., Jensen, J. A., Møller, H. S., Aaslyng, M. D., ... & Young, J. F. (2018). Classification of wooden breast myopathy in chicken pectoralis major by a standardised method and association with conventional quality assessments. International Journal of Food Science & Technology, 53(7), 1744-1752.

Davis, C. (1996). Lasers and Electro-optics: Fundamentals and Engineering. Cambridge University Press. New York, NY, USA.

de Almeida Mallmann, Barbara. (2019). Prediction and evaluation of breast myopathy. University of Arkansas.

Ding, C., & Peng, H. (2005). Minimum redundancy feature selection from microarray gene expression data. Journal of Bioinformatics and Computational Biology, 3(02), 185-205.

Ekramirad, N., Yoon, S. C., Bowker, B. C., & Zhuang, H. (2024). Nondestructive Assessment of Woody Breast Myopathy in Chicken Fillets Using Optical Coherence Tomography Imaging with Machine Learning: A Feasibility Study. Food and Bioprocess Technology, 1-18.

Ellsworth, S., Crandall, P. G., Seo, H. S., & O'Bryan, C. A. (2023). Consumers' willingness to pay for safer, more environmentally friendly smoke flavored chicken breasts. Journal of Sensory Studies, 38(2), e12812.

Feng, S., Chen, Q., Gu, G., Tao, T., Zhang, L., Hu, Y., ... & Zuo, C. (2019). Fringe pattern analysis using deep learning. Advanced photonics, 1(2), 025001-025001.

Geronimo, B. C., Mastelini, S. M., Carvalho, R. H., Júnior, S. B., Barbin, D. F., Shimokomaki, M., & Ida, E. I. (2019). Computer vision system and near-infrared spectroscopy for identification and classification of chicken with wooden breast, and physicochemical and technological characterization. Infrared Physics & Technology, 96, 303-310.

Gonzalez, R. C. & Woods, R. E. (2018). Digital Image Processing, 4th Edition. Pearson, New York, NY, USA.

Guo, Y., Hastie, T., & Tibshirani, R. (2007). Regularized linear discriminant analysis and its application in microarrays. Biostatistics, 8(1), 86-100.

He, K., Zhang, X., Ren, S., & Sun, J. (2016). Deep residual learning for image recognition. In Proceedings of the IEEE Conference on Computer Vision and Pattern Recognition, pp. 770-778.

Hu, M. K. (1962). Visual pattern recognition by moment invariants. IRE Transactions on Information Theory, 8(2), 179-187.

Huntley, J. M., & Saldner, H. (1993). Temporal phase-unwrapping algorithm for automated interferogram analysis. Applied optics, 32(17), 3047-3052.

Jolliffe, I. T. (2002). Principal Component Analysis. 2nd ed., Springer.

Kannala, J., & Rahtu, E. (2012). Bsif: Binarized statistical image features. In Proceedings of the 21st international conference on pattern recognition (ICPR2012), pp. 1363-1366.

Kienle, A., Lilge, L., Patterson, M. S., Hibst, R., Steiner, R., & Wilson, B. C. (1996). Spatially resolved absolute diffuse reflectance measurements for noninvasive determination of the optical scattering and absorption coefficients of biological tissue. Applied Optics, 35(13), 2304-2314.

Kuttappan, V. A., Hargis, B. M., & Owens, C. M. (2016). White striping and woody breast myopathies in the modern poultry industry: a review. Poultry Science, 95(11), 2724-2733.

Lee, Y. S., Owens, C. M., & Meullenet, J. F. (2008). A novel laser air puff and shape profile method for predicting tenderness of broiler breast meat. Poultry Science, 87 (7), 1451–1457.

Li, H., Sun, X., Pan, W., Kutsanedzie, F., Zhao, J., & Chen, Q. (2016). Feasibility study on nondestructively sensing meat's freshness using light scattering imaging technique. Meat Science, 119, 102-109.

Li, Z., Wu, L., Yang, Z., Zhang, Y., Wang, P., & Xu, X. (2022). Improved identification and classification accuracy of wooden breast by jointly using near-infrared spectroscopy and compression speed. Food Research International, 161, 111795.

Li, J., Lu, Y., & Lu, R. (2023). Detection of early decay in navel oranges by structured-illumination reflectance imaging combined with image enhancement and segmentation. Postharvest Biology and Technology, 196, 112162.

Li, J., Lu, Y., & Lu, R. (2024). Identification of early decayed oranges using structured-illumination reflectance imaging coupled with fast demodulation and improved image processing algorithms. Postharvest Biology and Technology, 207, 112627.

Li, R., Lu, Y., & Lu, R. (2018). Structured illumination reflectance imaging for enhanced detection of subsurface tissue bruising in apples. Transactions of the ASABE, 61(3), 809-819.

Liu, H., Yan, N., Shao, B., Yuan, S., Zhang, X. (2024). Deep learning in fringe projection: a review. Neurocomputing 581, 127493.

Lohumi, S., Cho, B. K., & Hong, S. (2021). LCTF-based multispectral fluorescence imaging: System development and potential for real-time foreign object detection in fresh-cut vegetable processing. Computers and Electronics in Agriculture, 180, 105912.

Lu, R. (2004a). Multispectral imaging for predicting firmness and soluble solids content of apple fruit. Postharvest Biology and Technology, 31(2), 147-157.

Lu, R. (2004b). Prediction of apple fruit firmness by near-infrared multispectral scattering. Journal of Texture Studies, 35(3), 263-276.

Lu, R., Van Beers, R., Saeys, W., Li, C., & Cen, H. (2020a). Measurement of optical properties of fruits and vegetables: A review. Postharvest Biology and Technology, 159, 111003.

Lu, Y., Li, R., & Lu, R. (2016a). Structured-illumination reflectance imaging (SIRI) for enhanced detection of fresh bruises in apples. Postharvest Biology and Technology, 117, 89-93.

Lu, Y., Li, R., & Lu, R. (2016b). Fast demodulation of pattern images by spiral phase transform in structured-illumination reflectance imaging for detection of bruises in apples. Computers and Electronics in Agriculture, 127, 652-658.

Lu, Y., & Lu, R. (2017). Histogram-based automatic thresholding for bruise detection of apples by structured-illumination reflectance imaging. Biosystems Engineering, 160, 30-41.

Lu, Y., Huang, Y., & Lu, R. (2017). Innovative hyperspectral imaging-based techniques for quality evaluation of fruits and vegetables: A review. Applied Sciences, 7(2), 189.

Lu, Y., & Lu, R. (2018a). Detection of surface and subsurface defects of apples using structured-illumination reflectance imaging with machine learning algorithms. Transactions of the ASABE, 61(6), 1831-1842.

Lu, Y., & Lu, R. (2018b). Fast Bi-dimensional empirical mode decomposition as an image enhancement technique for fruit defect detection. Computers and Electronics in Agriculture, 152, 314-323.

Lu, Y., & Lu, R. (2018c). Structured-illumination reflectance imaging coupled with phase analysis techniques for surface profiling of apples. Journal of Food Engineering, 232, 11-20.

Lu, Y., & Lu, R. (2019). Structured-illumination reflectance imaging for the detection of defects in fruit: Analysis of resolution, contrast and depth-resolving features. Biosystems engineering, 180, 1-15.

Lu, Y., Saeys, W., Kim, M., Peng, Y., & Lu, R. (2020b). Hyperspectral imaging technology for quality and safety evaluation of horticultural products: A review and celebration of the past 20-year progress. Postharvest Biology and Technology, 170, 111318.

Lu, Y., & Lu, R. (2020). Enhancing chlorophyll fluorescence imaging under structured illumination with automatic vignetting correction for detection of chilling injury in cucumbers. Computers and electronics in agriculture, 168, 105145.

Lu, Y., & Lu, R. (2021). Detection of chilling injury in pickling cucumbers using dual-band chlorophyll fluorescence imaging. Foods, 10(5), 1094.

Lu, Y., Lu, R., & Zhang, Z. (2021). Detection of subsurface bruising in fresh pickling cucumbers using structured-illumination reflectance imaging. Postharvest Biology and Technology, 180, 111624.

Lu, Y., & Cai, J. (2023). Structured-Light Imaging. In Zhang, Q. (eds), Encyclopedia of Smart Agriculture Technologies. New York: Springer, Cham.

Marangoni, F., Corsello, G., Cricelli, C., Ferrara, N., Ghiselli, A., Lucchin, L., & Poli, A. (2015). Role of poultry meat in a balanced diet aimed at maintaining health and wellbeing: an Italian consensus document. Food & Nutrition Research, 59(1), 27606.

McGlone, V. A., Abe, H., & Kawano, S. (1997). Kiwifruit firmness by near infrared light scattering. Journal of Near Infrared Spectroscopy, 5(2), 83-89.

Mery, D. (2011): BALU: A Matlab toolbox for computer vision, pattern recognition and image processing. http://dmery.ing.puc.cl/index.php/balu

Morey, A. & Owens, C. M. (2017). Methods for measuring meat texture. In Poultry Quality Evaluation, pp. 115-132. Woodhead Publishing.

Modzelewska-Kapituła, M., & Jun, S. (2022). The application of computer vision systems in meat science and industry–A review. Meat science, 192, 108904.

NCC. (2022a). Per Capita Consumption of Poultry and Livestock, 1965 to Forecast 2022, in Pounds. National Chicken Council. Retrieved from: https://www.nationalchickencouncil.org/about-the-industry/statistics/per-capita-consumption-of-poultry-and-livestock-1965-to-estimated-2012-in-pounds/

NCC. (2022b). U.S. Broiler Performance, 2022. National Chicken Council. Retrieved from: https://www.nationalchickencouncil.org/about-the-industry/statistics/u-s-broiler-performance/

Noh, H. K., & Lu, R. (2007). Hyperspectral laser-induced fluorescence imaging for assessing apple fruit quality. Postharvest Biology and Technology, 43(2), 193-201.

Ojala, T., Pietikäinen, M., & Harwood, D. (1996). A comparative study of texture measures with classification based on featured distributions. Pattern recognition, 29(1), 51-59.

Ojala, T., Pietikainen, M., & Maenpaa, T. (2002). Multiresolution gray-scale and rotation invariant texture classification with local binary patterns. IEEE Transactions on pattern analysis and machine intelligence, 24(7), 971-987.

Olaniyi, E. O., Lu, Y., Cai, J., Sukumaran, A. T., Jarvis, T., & Rowe, C. (2023a). Feasibility of imaging under structured illumination for evaluation of white striping in broiler breast fillets. Journal of Food Engineering, 342, 111359.

Olaniyi, E., Lu, Y., Sukumaran, A. T., Jarvis, T., & Rowe, C (2023b). Non-destructive assessment of white striping in broiler breast meat using structured-illumination reflectance imaging with deep learning. Journal of the ASABE, 66(6), 1437-1447.

Olaniyi, E. O., Lu, Y., Zhang, X., Sukumaran, A. T., Thames, H. T., & Pokhrel, D. (2024). Non-Destructive Assessment of Microbial Spoilage of Broiler Breast Meat Using Structured Illumination Reflectance Imaging with Machine Learning. Food Analytical Methods, 1-12.

Pang, B., Bowker, B., Yang, Y., Zhang, J., & Zhuang, H. (2020). Relationships between instrumental texture measurements and subjective woody breast condition scores in raw broiler breast fillets. Poultry Science, 99(6), 3292-3298.

Park, B. (2016). Quality evaluation of poultry carcass. In Computer vision technology for food quality evaluation, pp. 213-241.

Parajuli, P., Yoon, S. C., Zhuang, H., & Bowker, B. (2024). Characterizing the spatial distribution of woody breast condition in broiler breast fillet by compression force measurement. Journal of Food Measurement and Characterization, 18(3), 1991-2003.

Pallerla, C., Feng, Y., Owens, C. M., Bist, R. B., Mahmoudi, S., Sohrabipour, P., ... & Wang, D. (2024). Neural Network Architecture Search Enabled Wide-Deep Learning (NAS-WD) for Spatially Heterogenous Property Awared Chicken Woody Breast Classification and Hardness Regression. arXiv preprint arXiv:2409.17210.

Peng, Y., & Lu, R. (2006a). Improving apple fruit firmness predictions by effective correction of multispectral scattering images. Postharvest Biology and Technology, 41(3), 266-274.

Peng, Y., & Lu, R. (2006b). An LCTF-based multispectral imaging system for estimation of apple fruit firmness: Part I. Acquisition and characterization of scattering images. Transactions of the ASABE, 49(1), 259-267.

Peng, Y., & Lu, R. (2006c). An LCTF-based multispectral imaging system for estimation of apple fruit firmness: Part II. Selection of optimal wavelengths and development of prediction models. Transactions of the ASABE, 49(1), 269-275.

Peng, Y., & Lu, R. (2007). Prediction of apple fruit firmness and soluble solids content using characteristics of multispectral scattering images. Journal of Food Engineering, 82(2), 142-152.

Peng, Y., & Lu, R. (2008). Analysis of spatially resolved hyperspectral scattering images for assessing apple fruit firmness and soluble solids content. Postharvest Biology and Technology, 48(1), 52-62.

Petracci, M., Mudalal, S., Soglia, F., & Cavani, C. (2015). Meat quality in fast-growing broiler chickens. World's Poultry Science Journal, 71(2), 363-374.

Qin, J., & Lu, R. (2007). Measurement of the absorption and scattering properties of turbid liquid foods using hyperspectral imaging. Applied Spectroscopy, 61(4), 388-396.

Qin, J., Chao, K., Kim, M. S., Lu, R., & Burks, T. F. (2013). Hyperspectral and multispectral imaging for evaluating food safety and quality. Journal of Food Engineering, 118(2), 157-171.

Qin, J., Kim, M. S., Chao, K., Chan, D. E., Delwiche, S. R., & Cho, B. K. (2017). Line-scan hyperspectral imaging techniques for food safety and quality applications. Applied Sciences, 7(2), 125.

Ranasinghesagara, J., Nath, T. M., Wells, S. J., Weaver, A. D., Gerrard, D. E., & Yao, G. (2010). Imaging optical diffuse reflectance in beef muscles for tenderness prediction. Meat Science, 84(3), 413-421.

Siddique, A., Shirzaei, S., Smith, A. E., Valenta, J., Garner, L. J., & Morey, A. (2021). Acceptability of artificial intelligence in poultry processing and classification efficiencies of different classification models in the categorisation of breast fillet myopathies. Frontiers in Physiology, 12, 712649.

Siddique, A., Herron, C. B., Valenta, J., Garner, L. J., Gupta, A., Sawyer, J. T., & Morey, A. (2022). Classification and feature extraction using supervised and unsupervised machine learning approach for broiler woody breast myopathy detection. Foods, 11(20), 3270.

Sihvo, H. K., Immonen, K., & Puolanne, E. (2014). Myodegeneration with fibrosis and regeneration in the pectoralis major muscle of broilers. Veterinary Pathology, 51(3), 619-623.

Soglia, F., Mudalal, S., Babini, E., Di Nunzio, M., Mazzoni, M., Sirri, F., ... & Petracci, M. (2016). Histology, composition, and quality traits of chicken Pectoralis major muscle affected by wooden breast abnormality. Poultry Science, 95(3), 651-659.

Soglia, F., Silva, A. K., Lião, L. M., Laghi, L., & Petracci, M. (2019). Effect of broiler breast abnormality and freezing on meat quality and metabolites assessed by 1 H-NMR spectroscopy. Poultry Science, 98(12), 7139-7150.

Stratis, D. N., Eland, K. L., Carter, J. C., Tomlinson, S. J., & Angel, S. M. (2001). Comparison of acousto-optic and liquid crystal tunable filters for laser-induced breakdown spectroscopy. Applied spectroscopy, 55(8), 999-1004.

Sun, H., Peng, Y., Zheng, X., Wang, W., & Zhang, J. (2019a). Comparative analysis of pork tenderness prediction using different optical scattering parameters. Journal of Food Engineering, 248, 1-8.

Sun, X., Maynard, C. J., Caldas-Cueva, J. P., Coon, C. N., & Owens, C. M. (2021). Using air deformation of raw fillet surfaces to identify severity of woody breast myopathy in broiler fillets. LWT, 141, 110904.

Sun, Y., Lu, R., Lu, Y., Tu, K., & Pan, L. (2019b). Detection of early decay in peaches by structured-illumination reflectance imaging. Postharvest Biology and Technology, 151, 68-78.

Taheri-Garavand, A., Fatahi, S., Omid, M., & Makino, Y. (2019). Meat quality evaluation based on computer vision technique: A review. Meat science, 156, 183-195.

Tatarenkov, D. A., & Buchatsky, A. N. (2018). Feature extraction from a depth map for human detection. In 2018 Systems of Signal Synchronization, Generating and Processing in Telecommunications, pp. 1-4.

Tijare, V. V., Yang, F. L., Kuttappan, V. A., Alvarado, C. Z., Coon, C. N., & Owens, C. M. (2016). Meat quality of broiler breast fillets with white striping and woody breast muscle myopathies. Poultry Science, 95(9), 2167-2173.

Tu, K., Jancsók, P., Nicolaï, B., & De Baerdemaeker, J. (2000). Use of laser-scattering imaging to study tomato-fruit quality in relation to acoustic and compression measurements. International journal of food science & technology, 35(5), 503-510.

USDA-ERS. (2024). USDA Agricultural Projections to 2033, 2024. Retrieved from: https://www.ers.usda.gov/publications/pub-details/?pubid=108566

Vega, C., Marquez-Suarez, N., Leon, R., Castro-Fernandez, M., Socorro-Marrero, G. V., Fabelo, H., ... & Callico, G. M. (2024). Development and characterization of a hyperspectral LCTF-based colposcopic system. In Liquid Crystals Optics and Photonic Devices, Vol. 13016, pp. 70-80. SPIE.

Villegas-Cayllahua, E. A., de Mello, J. L. M., Dutra, D. R., de Oliveira, R. F., Cavalcanti, É. F., Pereira, M. R., ... & Borba, H. (2023). Effect of freezing on the quality of breast meat from broilers affected by wooden breast myopathy. Poultry Science, 102(8), 102702.

Vishwanath, K., Yuan, H., Barry, W. T., Dewhirst, M. W., & Ramanujam, N. (2009). Using optical spectroscopy to longitudinally monitor physiological changes within solid tumors. Neoplasia, 11(9), 889-900.

Wang, Y., Xu, H., Zhu, H., Chen, X., & Wang, Y. (2023). Pixel-wise phase unwrapping with adaptive reference phase estimation for 3-D shape measurement. IEEE Transactions on Instrumentation and Measurement, 72, 1-9.

Williams, J. (2024). The Effects of Multiple Further Processing Techniques on Objective Textural Characteristics of Woody Breasted Fillets. University of Georgia.

Wold, J. P., Veiseth-Kent, E., Høst, V., & Løvland, A. (2017). Rapid on-line detection and grading of wooden breast myopathy in chicken fillets by near-infrared spectroscopy. PLoS One, 12(3), e0173384.

Wold, J. P., Måge, I., Løvland, A., Sanden, K. W., & Ofstad, R. (2019). Near-infrared spectroscopy detects woody breast syndrome in chicken fillets by the markers protein content and degree of water binding. Poultry Science, 98(1), 480-490.

Wold, J. P., & Løvland, A. (2020). NIR spectroscopic techniques for quality and process control in the meat industry. Meat and Muscle Biology, 4(2).

Wu, J., Peng, Y., Li, Y., Wang, W., Chen, J., & Dhakal, S. (2012). Prediction of beef quality attributes using VIS/NIR hyperspectral scattering imaging technique. Journal of Food Engineering, 109(2), 267-273.

Xia, J., Weaver, A., Gerrard, D. E., & Yao, G. (2008). Distribution of optical scattering properties in four beef muscles. Sensing and Instrumentation for Food Quality and Safety, 2, 75-81.

Xie, S., Girshick, R., Dollár, P., Tu, Z., & He, K. (2017). Aggregated residual transformations for deep neural networks. In Proceedings of the IEEE Conference on Computer Vision and Pattern Recognition, pp. 1492-1500.

Xing, T., Zhao, X., Zhang, L., Li, J. L., Zhou, G. H., Xu, X. L., & Gao, F. (2020). Characteristics and incidence of broiler chicken wooden breast meat under commercial conditions in China. Poultry Science, 99(1), 620-628.

Xiong, R., Cavitt, L. C., Meullenet, J. F., & Owens, C. M. (2006). Comparison of Allo–Kramer, Warner–Bratzler and razor blade shears for predicting sensory tenderness of broiler breast meat. Journal of Texture Studies, 37(2), 179-199.

Xu, J., Lu, Y., Olaniyi, E., & Harvey, L. (2024). Online volume measurement of sweetpotatoes by A LiDAR-based machine vision system. Journal of Food Engineering, 361, 111725.

Yang, G., Zheng, Z., Li, H., & Liu, X. (2010). Method to reduce sidelobes of multistage Lyot filters. Applied optics, 49(8), 1280-1287.

Yang, Y., Wang, W., Zhuang, H., Yoon, S. C., Bowker, B., Jiang, H., & Pang, B. (2021). Evaluation of broiler breast fillets with the woody breast condition using expressible fluid measurement combined with deep learning algorithm. Journal of Food Engineering, 288, 110133.

Yoon, S. C., Bowker, B. C., & Zhuang, H. (2016). Toward a fusion of optical coherence tomography and hyperspectral imaging for poultry meat quality assessment. Electronic Imaging, 2016(14), 1-5.

Yoon, S. C., Bowker, B. C., Zhuang, H., & Lawrence, K. C. (2022). Development of imaging system for online detection of chicken meat with wooden breast condition. Sensors, 22(3), 1036.

Zahn, C. T., & Roskies, R. Z. (1972). Fourier descriptors for plane closed curves. IEEE Transactions on Computers, 100(3), 269-281.

Zhang, S. (2018a). High-speed 3D shape measurement with structured light methods: A review. Optics and lasers in engineering, 106, 119-131.

Zhang, S. (2018b). Absolute phase retrieval methods for digital fringe projection profilometry: A review. Optics and lasers in engineering, 107, 28-37.

Zhang, T., Gao, X., & Li, J. (2020). The improved Hu moment and its application in gesture recognition. In 2020 International Conference on Computer Vision, Image and Deep Learning (CVIDL), pp. 577-580.

Zhao, H., Chen, W., & Tan, Y. (1994). Phase-unwrapping algorithm for the measurement of three-dimensional object shapes. Applied optics, 33(20), 4497-4500.

Zuo, C., Feng, S., Huang, L., Tao, T., Yin, W., & Chen, Q. (2018). Phase shifting algorithms for fringe projection profilometry: A review. Optics and lasers in engineering, 109, 23-59.

Zuo, R., Wei, S., Wang, Y., Kam, M., Opfermann, J.D., Hsieh, M.H., Krieger, A., Kang, J.U. (2024). Deep learning-based single-shot fringe projection profilometry. Advanced Biomedical and Clinical Diagnostic and Surgical Guidance Systems XXII 1283106.